Dynamical well-killing simulation of a vertical H2S-containing natural gas well

Liangjie Mao, Mingjie Cai, Qingyou Liu, Guorong Wang

Oil & Gas Science and Technology – Rev. IFP Energies nouvelles **75**, 71 (2020)
© L. Mao et al., published by IFP Energies nouvelles, 2020
https://doi.org/10.2516/ogst/2020065

Available online at:
ogst.ifpenergiesnouvelles.fr

REGULAR ARTICLE OPEN ACCESS

Dynamical well-killing simulation of a vertical H_2S-containing natural gas well

Liangjie Mao[1,2,*], Mingjie Cai[1,2], Qingyou Liu[1,*], and Guorong Wang[1]

[1] State Key Laboratory of Oil and Gas Reservoir Geology and Exploitation, Southwest Petroleum University, Sichuan, Chengdu 610500, China
[2] Petroleum Engineering School, Southwest Petroleum University, Sichuan, Chengdu 610500, China

Received: 3 March 2020 / Accepted: 27 August 2020

Abstract. This work aims to explore the dynamical well-killing process of a vertical H_2S-containing natural gas well. A dynamical well-killing model considering an H_2S solubility was established to simulate the overflow and well-killing process of a vertical H_2S-containing natural gas well. The mass and momentum equations of the coupled model were solved using finite difference method, while the transient temperature prediction model was solved using finite volume method. The coupled model was validated by reproducing experimental data and field data of Well Tiandong #5. The effect of H_2S content, mud displacement, drilling fluid density, and initial overflow volume on the dynamical well-killing process of an H_2S-containing natural gas well were obtained and analyzed in this work. Results showed that H_2S will gasify near wellhead during well killing when casing pressure decreases. To balance the bottom hole pressure, when H_2S releases, the casing pressure increases as H_2S content increases. As initial overflow volume increases, the annular temperature, annular pressure and the casing pressure increase significantly. When H_2S gasifies, the casing pressure applied at wellhead should be higher at lower initial overflow volume to balance bottom hole pressure. In the well-killing process, the annular pressure and temperature decrease as drilling fluid density increases and a lower casing pressure is needed for balancing bottom hole pressure. The casing pressure is lower at a higher displacement for higher friction resistance. Besides, as well-killing displacement increases H_2S will gasify at an earlier time. When drilling for H_2S-containing natural gas well, early detection of gas kick should be more frequent to avoid severe overflow. Besides, higher displacement and density of drilling fluid should be considered to avoid stratum fracturing and prevent leakage accidents under the premise of meeting drilling requirements.

Nomenclature

Q_g	Gas production
Q_{g-H_2S}	Released H_2S
ρ_g	Densities of gas
ρ_l	Density of drilling fluid
v_g	Velocity of gas
v_l	Velocity of drilling fluid
E_g	Gas void fraction
E_l	Liquid holdup
A	Cross-sectional area
g	Local acceleration of gravity
$\left(\frac{\partial P}{\partial z}\right)_{fr}$	Friction pressure drop
c_1	Specific heat capacity of the drilling fluid in the drilling string
T_1	Drilling fluid temperature in the drilling string
u_p	Velocity in the x direction of the drilling fluid in the drilling string
v_p	Velocity in the y direction of the drilling fluid in the drilling string
Γ_x	Heat transfer coefficient of the drilling fluid in the x direction
Γ_y	Heat transfer coefficient of the drilling fluid in the y direction
ρ_2	Density of the drilling string
T_2	Drilling string temperature
h	Well depth
Q_l	Mud displacement
V_{pg}	Pit gain at shut-in time
P_0	Wellhead pressure
P_p	Formation pressure
v_{sg}	Superficial velocities of gas
v_{sl}	Superficial velocities of liquid

* Correspondence authors: maoliangjie@qq.com; liuqy66@aliyun.com

v_{oo}	Gas drift velocity
σ	Surface tension
k_1, k_2	Correction coefficients
y_i	Mole fractions of H_2S in the gas
x_i	Mole fractions of H_2S in the liquid
φ_i^V	Fugacity coefficients of H_2S in the gas
φ_i^l	Fugacity coefficients of H_2S in the liquid
k_{ij}	Interaction coefficient between H_2S and hydrocarbon components in natural gas
T_{ci}	Critical temperature of H_2S
P_{ci}	Critical pressure of H_2S
T_{ri}	Correspondent temperature of H_2S
w	Acentric factor of H_2S
D	Borehole size
d	Drill pipe diameter
v_{gr}	Drift velocity
C_0	Distribution coefficient
v_m	Mixed velocity of gas and liquid
Hr	Viscous friction head
D_e	Equivalent diameter
n	Flow index of the drilling fluid
R_e	Reynolds number of the mixed fluids
ε_e	Equivalent absolute roughness
P_b	Bottom hole pressure
r_w	Hole radius
K	Reservoir permeability
c	System compressibility
μ_g	Gas viscosity
t	Overflow time
W_g	Molar mass of natural gas
R	Molar gas constant
P_a	Casing pressure
P_{la}	Circulating pressure loss
P_{ma}	Hydrostatic pressure created by the fluid column
R_e	Mean Reynolds number of the mixed fluids
φ_i^v	Fugacity coefficients of H_2S in the gas
φ_i^l	Fugacity coefficients of H_2S in the liquid
Z	Natural gas compression factor

1 Introduction

Gas kick and well-killing are the main concerns of well control during the drilling of oil and gas fields. Various multiphase flow models have been proposed to predict the flow pattern distribution in the wellbore after gas kick (Amaya-Gómez *et al.*, 2019; Ansari *et al.*, 1994; Bilicki and Kestin, 1987; Ebrahimi and Khamehchi, 2015; Feng *et al.*, 2015; Guo *et al.*, 2018; Hasan and Kabir, 1988; Kelessidis and Dukler, 1989; Li and Mouline, 1997; Zhang *et al.*, 2019); among them, the most widely used in drilling engineering are the patterns of bubble, slug, churn, and annular flows (Osman, 2004; Raghavan, 1989; Sun *et al.*, 2017). On the basis of these studies, many researchers have focused on the multiphase flow in the wellbore under different conditions. Nickens (1987) proposed a dynamic computer model by a solution of the mass and momentum balance equations for predicting the dynamical two-phase flow behavior and pressure response of the wellbore. Sun and Wang proposed a mathematical model to predict the multiphase flow in a wellbore for deep water wells (Wang *et al.*, 2016). Their model has also been used to study the phase transition of hydrate during the exploitation of natural gas hydrate (Wang and Sun, 2009, 2014). Xu *et al.* (2018, 2019) developed a non-isothermal two-phase flow model to investigate the effect of major parameters on the two-phase flow behavior in the wellbore. They found that temperature, pressure, and solubility fields are mutually influential. The gas solubility effect and heat transfer effect influence gas kick characteristics significantly. Meng *et al.* (2015) proposed a transient gas–liquid drift flux model based on Shi slip relation for simulating gas kick/injection and solved the model numerically using finite volume method and advection upstream splitting method V scheme. Xie *et al.* (2014) established a transient model to study the changing rule of wellhead parameters during blowout and found that the gas outlet velocity increases as well depth increases. Hou *et al.* (2019) conducted an experiment to study the heat transfer for gas-liquid two-phase flow in wellbore and developed a new model of convective heat transfer coefficient. Fu *et al.* (2019) proposed the mathematic model of wellbore annulus transient water hammer with the consideration of transient multi-phase flow characteristics and pointed out that both the additional water hammer pressure and shut-in casing pressure generated by the closure of BOP are likely to cause formation at the shallow casing shoe damage.

With the increasing demand for natural gas, an increasing number of gas reservoirs that contain H_2S will be drilled (Guo and Wang, 2016; Yin *et al.*, 2015; Zhang *et al.*, 2020; Zhu *et al.*, 2011). The existing states of H_2S are greatly affected by temperature and pressure. The state may transform from supercritical to gas in the wellbore as annular pressure and temperature decrease, and this condition influences annular pressure and flow pattern distribution. Therefore, the typical gas–liquid two-phase flow models may be unsuitable for predicting the multiphase flow behavior in H_2S-containing natural gas wells. The "12·23" Gas Blowout Accident in Kaixian County, Chongqing has elicited scholarly attention on phase transition of H_2S in well control. Some scholars have focused on multiphase flow behavior of H_2S-containing natural gas wells. Sun and Wang *et al.* established a multiphase flow model that considers the phase change of the H_2S in the drilling fluid; simulation results showed that, as the invasion gas moves up along the wellbore to the critical position of H_2S, the released H_2S may cause a rapid volume expansion, thereby increasing the blowout risk (Sun *et al.*, 2013, 2018).

It can be seen that most of the existing studies are focused on the gas kick simulation of a well and, the well-killing simulation after gas kick is scarce, especially for an H_2S-containing natural gas well. By applying casing pressure in the wellhead during well killing, the two-phase flow behavior is different from that in the overflow (gas kick). Thus, the phase change behavior of H_2S may be different from that described in the abovementioned published

literature. Thus, it is of significance to study the well-killing process of an H_2S-containing natural gas well to offer a guidance for exploitation of H_2S-containing gas reservoir.

Thus, the aim of this study is to establish a dynamical well-killing model considering an H_2S solubility to simulate the overflow and well-killing process of a vertical H_2S-containing natural gas well. The mass and momentum equations of the coupled model were solved using finite difference method, while the transient temperature prediction model was solved using finite volume method. The continuity and momentum equations are decoupled from temperature prediction model. The effect of H_2S content, mud displacement, drilling fluid density, and initial overflow volume on the dynamical well-killing process of an H_2S-containing natural gas well were obtained and analyzed in this work.

2 Mathematical model

2.1 Governing equations for mass and momentum

During drilling, gas enters the wellbore from the stratum when overflow occurs, and gas–liquid two-phase flow appears below the location the gas reaches. Given that two-phase flow exists in overflow and well-killing periods, a mathematical model is established in this work to obtain the two-phase flow behavior.

To simplify the calculation, the following assumptions are made in this work:

1. The gas and drilling fluid flow in a vertical wellbore is considered one dimensional;
2. The compressibility of the drilling fluid is ignored;
3. Gas and liquid phases are continuous in the control unit;
4. The influence of annulus eccentricity is disregarded;
5. The geothermal gradient is regarded as constant.

Then, the continuity equations of gas and liquid phases are expressed as follows (Wei *et al.*, 2018):

$$\frac{\partial(\rho_g v_g E_g A)}{\partial z}+\frac{\partial(\rho_g E_g A)}{\partial t}=\begin{cases} Q_g+Q_{g-H_2S}(\text{overflow period}) \\ Q_{g-H_2S}(\text{well killing period}) \end{cases}, \tag{1}$$

$$\frac{\partial(\rho_l v_l E_l A)}{\partial z}+\frac{\partial(\rho_l E_l A)}{\partial t}=0. \tag{2}$$

On the basis of the law of conservation of momentum, the momentum equation can be obtained as follows:

$$\frac{\partial}{\partial t}(\rho_l v_l E_l+\rho_g v_g E_g)+\frac{\partial}{\partial z}(\rho_l v_l^2 E_l+\rho_g v_g^2 E_g)+\frac{\partial P}{\partial z} +(\rho_l E_l+\rho_g E_g)g+\left(\frac{\partial P}{\partial z}\right)_{fr}=0. \tag{3}$$

2.2 Transient temperature prediction model

To accurately predict the phase change behavior of H_2S in wellbore, a transient temperature prediction model is developed (Mao and Zhang, 2018). The unsteady two-dimensional convection–diffusion and unsteady two-dimensional diffusion equations are used to describe the heat transfer models as follows:

(1) Heat transfer model in the drilling string:

$$\frac{\partial(\rho_1 c_1 T_1)}{\partial t}+\frac{\partial}{\partial x}(\rho_1 c_1 u_p T_1)+\frac{\partial}{\partial y}(\rho_1 c_1 v_p T_1) =\frac{\partial}{\partial x}\left(\Gamma_{1x} c_1 \frac{\partial T_1}{\partial x}\right)+\frac{\partial}{\partial y}\left(\Gamma_{1y} c_1 \frac{\partial T_1}{\partial y}\right)+S_p. \tag{4}$$

(2) Heat transfer model of drilling string:

$$\frac{\partial(\rho_2 c_2 T_2)}{\partial t}=\frac{\partial}{\partial x}\left(\Gamma_{2x} c_2 \frac{\partial T_2}{\partial x}\right)+\frac{\partial}{\partial y}\left(\Gamma_{2y} c_2 \frac{\partial T_2}{\partial y}\right). \tag{5}$$

(3) Heat transfer model in the annular:

$$\frac{\partial(\rho_3 c_3 T_3)}{\partial t}+\frac{\partial}{\partial x}(\rho_3 c_3 u_a T_3)+\frac{\partial}{\partial y}(\rho_3 c_3 v_a T_3) =\frac{\partial}{\partial x}\left(\Gamma_{3x} c_3 \frac{\partial T_3}{\partial x}\right)+\frac{\partial}{\partial y}\left(\Gamma_{3y} c_3 \frac{\partial T_3}{\partial y}\right)+S_a. \tag{6}$$

(4) Heat transfer model of casing, cement sheath, and formation:

$$\frac{\partial(\rho_i c_i T_i)}{\partial t}=\frac{\partial}{\partial x}\left(\Gamma_{ix} c_i \frac{\partial T_i}{\partial x}\right)+\frac{\partial}{\partial y}\left(\Gamma_{iy} c_i \frac{\partial T_i}{\partial y}\right). \tag{7}$$

2.2 Initial and boundary conditions

(1) Overflow period

When overflow occurs, the wellhead is open and the parameters under normal drilling conditions can be used as the initial conditions of a well kick:

$$\begin{cases} P(h,0)=P_b \\ Q(h,0)=Q_l \\ E_g(h,0)=0 \\ E_l(h,0)=1 \\ v_l(h,0)=Q_l/A \end{cases}. \tag{8}$$

The boundary conditions are shown as follows:

$$\begin{cases} P(0,t)=P_0 \\ Q(h,t)=Q_l+Q_g(h,t) \\ \mathrm{Pg}=V_{pg} \end{cases}. \tag{9}$$

(2) Killing period

After the shut-in operation is performed, the flow pattern, gas void fraction, and annular pressure distributions at the shut-in time can be considered the initial conditions of the well-killing period. During the well-killing process, the bottom hole pressure is equal to the formation pressure, and the boundary conditions are shown as follows:

$$\begin{cases} P(0,t) = P_{\mathrm{p}} \\ Q_{\mathrm{l}}(0,t) = Q_{\mathrm{l}}. \\ Q_{\mathrm{g}}(0,t) = 0 \end{cases} \tag{10}$$

2.3 Flow pattern discriminant

The main patterns of a gas–liquid two-phase flow are bubble, slug, churn, and annular flows (Hasan and Kabir, 1988). They can be discriminated by the following equations:

Bubble flow:

$$v_{\mathrm{sg}} \le k_1 \times (0.429 \times v_{\mathrm{sl}} + 0.357 \times v_{\mathrm{oo}}), \tag{11}$$

$$v_{\mathrm{oo}} = 1.53\left[\frac{g(\rho_{\mathrm{l}} - \rho_{\mathrm{g}})\sigma}{{\rho_{\mathrm{l}}}^2}\right]^{0.25}. \tag{12}$$

Slug flow:

$$v_{\mathrm{sg}} > k_1 \times (0.429 \times v_{\mathrm{sl}} + 0.357 \times v_{\mathrm{oo}}). \tag{13}$$

Churn flow:

$$\begin{cases} v_{\mathrm{sg}} < 3.1\left[\frac{g(\rho_{\mathrm{l}} - \rho_{\mathrm{g}})\sigma}{\rho_{\mathrm{g}}^2}\right]^{0.25} \\ \rho_{\mathrm{g}} v_{\mathrm{g}}^2 > 25.41 g\left(\rho_{\mathrm{l}} v_{\mathrm{sl}}^2\right) - 39 \rightarrow if\, \rho_{\mathrm{l}} v_{\mathrm{sl}}^2 > 74.4 \cdot \\ \rho_{\mathrm{g}} v_{\mathrm{g}}^2 > 0.0051(\rho_{\mathrm{l}} v_{\mathrm{sl}}^2)^{1.7} \rightarrow if \rho_{\mathrm{l}} v_{\mathrm{sl}}^2 \le 74.4 \end{cases} \tag{14}$$

Annular flow:

$$v_{\mathrm{sg}} > 3.1\left[\frac{g(\rho_{\mathrm{l}} - \rho_{\mathrm{g}})\sigma}{\rho_{\mathrm{g}}^2}\right]^{0.25}. \tag{15}$$

2.4 Calculation of key parameters

2.4.1 H_2S solubility

The solubility of H_2S in the drilling fluid can be expressed as (Sun *et al.*, 2018):

$$x_i = \frac{p y_i \varphi_i^v}{p \varphi_i^{\mathrm{l}}}, \tag{16}$$

$$P = \frac{RT}{V - b} - \frac{a}{V(V + b) + b(V - b)}. \tag{17}$$

With $A = \frac{ap}{R^2 T^2}$, $B = \frac{bp}{RT}$, and $Z = \frac{PV}{RT}$, equation (13) can be written as

$$Z^3 - (1 - B)Z^2 + (A - 3B^2 - 2B)Z - (AB - B^2 - B^3) = 0, \tag{18}$$

$$a = \sum_i \sum_j x_i x_j \sqrt{\alpha_i \alpha_j}\left(1 - k_{ij}\right), \tag{19}$$

$$b = \sum_i x_i \frac{0.0778 R T_{\mathrm{ci}}}{P_{\mathrm{ci}}}, \tag{20}$$

$$\alpha_i = \left[1 + m(1 - T_{\mathrm{ri}}^{0.5})\right]^2, \tag{21}$$

$$\alpha_j = \frac{0.45724 R^2 T_{\mathrm{ci}}^2}{P_{\mathrm{ci}}} \alpha_i, \tag{22}$$

and

$$m = 0.37464 + 1.5226 - 0.26992 w^2. \tag{23}$$

Thus, the fugacity coefficient of a certain component is expressed as:

$$\ln \varphi_i = \frac{b_i}{b}(Z - 1) - \ln(Z - b) - \frac{a}{2\sqrt{2}b}\left(\frac{2\sum_j x_i \alpha_{ij}}{a} - \frac{b_i}{b}\right) \times \ln\left[\frac{Z + (1 + \sqrt{2})b}{Z + 12\sqrt{2}b}\right]. \tag{24}$$

The solubility of H_2S in the liquid can be obtained by combining equation (16) with equation (24).

2.4.2 Drift flux model

In the drift flux model, the corresponding slip rate of the gas phases and distribution coefficient in case of different flow patterns are shown as follows (Wei *et al.*, 2018):

Bubble flow:

$$v_{\mathrm{gr}} = 1.53\left(\frac{g(\rho_{\mathrm{l}} - \rho_{\mathrm{g}})\sigma}{{\rho_{\mathrm{l}}}^2}\right)^{0.25}, \tag{25}$$

$$C_0 = 1.20 + 0.371 \times \frac{d}{D}. \tag{26}$$

Slug flow:

$$v_{\mathrm{gr}} = 0.35\left(\frac{gD(\rho_{\mathrm{l}} - \rho_{\mathrm{g}})}{\rho_{\mathrm{l}}}\right)^{0.5}, \tag{27}$$

$$C_0 = 1.182 + 0.9 \times \frac{d}{D}. \tag{28}$$

Churn and annular flows:

$$v_{\mathrm{gr}} = \left(0.35 + 0.22\frac{D}{d}\right)\left(\frac{g(D-d)(\rho_{\mathrm{l}} - \rho_{\mathrm{g}})}{\rho_{\mathrm{l}}}\right)^{0.5}, \quad C_0 = 1. \tag{29}$$

Thus, the gas void fraction can be calculated by the following equations:

$$E_{\mathrm{g}} = \frac{v_{\mathrm{sg}}}{C_o v_{\mathrm{m}} + v_{\mathrm{gr}}}, \tag{30}$$

$$v_{\mathrm{m}} = v_{\mathrm{sg}} + v_{\mathrm{sl}}, \tag{31}$$

2.4.3 Friction pressure drop

For single phase flow, the friction pressure drop can be obtained using the friction factor of the power-law fluid.

$$Hr = 2f{v_l}^2\rho_l/D_e, \tag{32}$$

$$\begin{cases} f = \dfrac{8}{v_l^2\rho_l}\left[\dfrac{8v_l}{D_e}\dfrac{3n+1}{4n}\right]^n, \quad \text{if Re 2000} \\ \dfrac{1}{\sqrt{f}} = \dfrac{2.1}{n^{0.75}}\log\left[\mathrm{Re}\left(\dfrac{f}{4}\right)^{1-n/2}\right] - \dfrac{0.2}{n^{1.2}} > 2000. \end{cases} \tag{33}$$

For gas–liquid two-phase flow, the friction pressure drop can be calculated using the following equations established by Yin *et al.* (2017).

Bubble flow:

$$Hr = 2f{v_m}^2\rho_m/D_e, \tag{34}$$

$$\begin{cases} \dfrac{1}{\sqrt{f}} = -4\log\left(\dfrac{\varepsilon_e}{3.71D_e} - \dfrac{5.05\log A}{\mathrm{Re}}\right), \\ A = m\times\left(\dfrac{\varepsilon_e}{2.56D_e}\right)^{1.11} + \left(\dfrac{7.149}{\mathrm{Re}}\right)^{0.898}. \end{cases} \tag{35}$$

Slug flow:

$$Hr = 2(1-E_g)f{v_m}^2\rho_m/D_e \tag{36}$$

$$\begin{cases} \dfrac{1}{\sqrt{f}} = -4\log\left(\dfrac{\varepsilon_e}{3.71D_e} - \dfrac{5.05\log A}{Re}\right) \\ A = \left(\dfrac{\varepsilon_e}{2.56D_e}\right)^{1.11} + \left(\dfrac{7.149}{Re}\right)^{0.898} \end{cases} \tag{37}$$

Churn and annular flows:

$$Hr = 2fv_m^2\rho_m/(D_eE_g^2) \tag{38}$$

$$f = 0.079\left[1+75(1-E_g)\right]/(\mathrm{Re}g^{0.25}) \tag{39}$$

2.4.4 Gas production

Under the effect of pressure differential between bottom hole and formation pressures, the H_2S-containing natural gas enters the wellbore. In this work, the following equation is adopted to calculate gas production (Elsharkawy, 2004):

$$Q_g = \frac{2.64\times10^{-20}\mathrm{Kh}(P_p^2 - P_b^2)}{(0.8+\mathrm{Int_D})\left[(T-255)Z\mu_g\right]}, \tag{40}$$

$$t_D = \max\left\{10, \frac{1.47\times10^{-9}t}{{r_w}^2}\left(\frac{K}{c\phi\mu_g}\right)\right\}. \tag{41}$$

2.4.5 Gas density

The gas density can be described by introducing a compression factor into the ideal gas equation, as defined in the equation below (Yin *et al.*, 2017):

$$\rho_g = \frac{PW_g}{ZRT}. \tag{42}$$

2.4.6 Convective heat transfer coefficients

Convective heat transfer coefficients can be expressed as follows (Mao and Zhang, 2018):

$$h = \frac{\mathrm{Nu}\cdot\lambda}{d}. \tag{43}$$

For laminar flow, Nu = 4.36; for turbulent flow, Nu = 0.023 $\mathrm{Re}^{0.8}$ $\mathrm{Pr}^{0.33}$.

3 Model solution

3.1 Solution for mass and momentum governing equations

The finite difference method is used in this work to solve the mass and momentum governing equations. Meanwhile, the influence of the boundary and initial conditions in each control region are considered in the solving model. The solution is completed by three steps: generating discrete grids, constructing discrete equations, and solving these equations.

(1) Generating discrete grids

In finite difference numerical calculation, the spatial domain is the wellbore. For the overflow simulation, the time domain is the entire time from the overflow to the shut-in. For the well-killing simulation, the time domain is from the shut-in to the time the lower boundary of two-phase reaches wellhead. The schematic of discrete grid nodes of the wellbore is shown in Figure 1a.

(2) Model discretization

Figure 1b shows the cell grid integration area K. The partial differential equation in the mathematical model can be written as

$$\frac{\partial X}{\partial t} + \frac{\partial Y}{\partial z} = 0. \tag{44}$$

Then, by integrating this equation into area K, a curvilinear integral along the boundary of L can be obtained in accordance with Green's theorem:

$$\begin{aligned} &\iint\left(\frac{\partial X}{\partial t}+\frac{\partial Y}{\partial z}\right)\mathrm{d}t\mathrm{d}z = \int_L X\mathrm{d}z - Y\mathrm{d}t = \int_{L1} + \int_{L2} + \int_{L3} + \int_{L4} \\ &= -\int_{t(i)}^{t(i+1)} Y(t,z(j))\mathrm{d}t + \int_{z(j)}^{z(j+1)} X(t(i+1),z)\mathrm{d}z \\ &\quad + \int_{t(i)}^{t(i+1)} Y(t,z(j+1))\mathrm{d}t - \int_{z(j)}^{z(j+1)} X(t(i),z)\mathrm{d}z = 0. \end{aligned} \tag{45}$$

The above-mentioned equation can be converted to the following equation by simplification:

$$Y_{i+1}^{j+1} - Y_{i+1}^{j} = \frac{\Delta z}{2\Delta t}\left(X_j^i + X_{j+1}^i - X_j^{i+1} - X_{j+1}^{i+1}\right), \tag{46}$$

(3) Numeralization of the continuity equation

For gas-phase continuity equation, we let

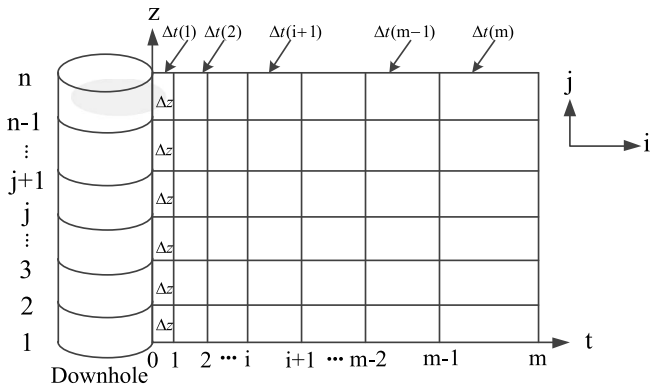

(a) Schematic of discrete grid nodes of the wellbore.

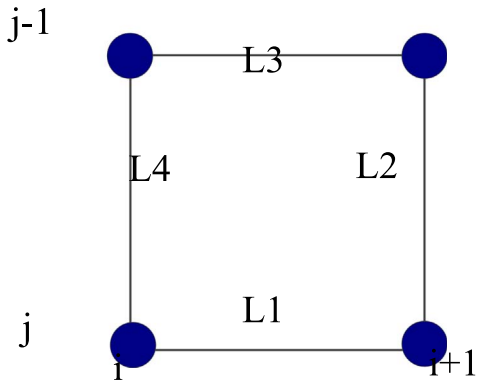

(b) Diagram of cell grid integration area K

Fig. 1. Schematic diagram of solution for the mass and momentum equations: (a) Schematic of discrete grid nodes of the wellbore; (b) Diagram of cell grid integration area *K*.

$$\begin{cases} X = \rho_g E_g, \\ Y = \rho_g E_g v_g. \end{cases} \tag{47}$$

Thus, the gas-phase difference equation can be obtained by combining equations (46) and (47):

$$\left[(\rho_g V_g E_g)_{i+1}^{j+1} - (\rho_g V_g E_g)_i^{j+1}\right] = 0.5\Delta z/\Delta t\Big[(\rho_g E_g)_i^j + (\rho_g E_g)_i^{j+1} - (\rho_g E_g)_j^{i+1} - (\rho_g E_g)_{i+1}^{j+1}\Big] + 0.5\Delta z\Big(Q_{g-H_2S}{}_{i+1}^{j+1} + Q_{g-H_2S}{}_{i+1}^{j}\Big) \tag{48}$$

Similarly, the liquid-phase difference equation can be obtained as follows:

$$\left[(\rho_l V_l E_l)_{i+1}^{j+1} - (\rho_l V_l E_l)_i^{j+1}\right] = 0.5\Delta z/\Delta t\Big[(\rho_l E_l)_i^j + (\rho_l E_l)_i^{j+1} - (\rho_l E_l)_j^{i+1} - (\rho_l E_l)_{i+1}^{j+1}\Big]. \tag{49}$$

(4) Numeralization of the momentum equation
For mixed momentum equation, we let

$$\begin{cases} X = \rho_g E_g v_g + \rho_l E_l v_l, \\ Y = \rho_g E_g v_g{}^2 + \rho_l E_l v_l{}^2 + \rho_g E_g + \rho_l E_l g + P + P_{fr}. \end{cases} \tag{50}$$

Thus, the mixed momentum difference equation can be obtained by combining equations (46) and (50):

$$\begin{aligned} P_{i+1}^{j+1} - P_{i+1}^{j} = \frac{\Delta z}{2\Delta t}\{&[(\rho_l v_l E_l + \rho_g v_g E_g)]_i^j + [(\rho_l v_l E_l \\ &+ \rho_g v_g E_g)]_{i+1}^{j+1} - [(\rho_l v_l E_l + \rho_g v_g E_g)]_{i+1}^{j} - [(\rho_l v_l E_l \\ &+ \rho_g v_g E_g)]_{i+1}^{j+1}\} + (\rho_l v_l^2 E_l + \rho_g v_g^2 E_g)_{i+1}^{j} \\ &- 0.5\Delta z g(\rho_l E_l + \rho_g E_g)_{i+1}^{j} + -(\rho_l v_l^2 E_l \\ &+ \rho_g v_g^2 E_g)_{i+1}^{j+1} - 0.5\Delta z g(\rho_l E_l + \rho_g E_g)_{i+1}^{j+1} \\ &- 0.5\Delta z\left[\left(\frac{\partial P}{\partial z}\right)_{fr}\right]_{i+1}^{j} - 0.5\Delta z\left[\left(\frac{\partial P}{\partial z}\right)_{fr}\right]_{i+1}^{j+1}. \end{aligned} \tag{51}$$

3.2 Solution for transient temperature prediction model

Figure 2 shows the grid diagram of the wellbore and formation. By using finite volume method, equations (4)–(7) can be expressed as (Mao and Zhang, 2018):

$$j = 1 \quad a_P T_P = a_{NN} T_{NN} + a_N T_N + a_W T_W + a_S T_S + a_E T_E + b, \tag{52}$$

$$j = 2 \quad a_P T_P = a_N T_N + a_W T_W + a_S T_S + a_E T_E + b, \tag{53}$$

$$j = 3 \quad a_P T_P = a_{SS} T_{SS} + a_N T_N + a_W T_W + a_S T_S + a_E T_E + b, \tag{54}$$

$$j \le 4 \quad a_P T_P = a_N T_N + a_W T_W + a_S T_S + a_E T_E + b. \tag{55}$$

By using under-relaxation iteration method, discretized scheme of the heat transfer control equations are obtained as follows:

See equations (56)–(59) top of next page

Figure 3 shows the flow chart of model solution.

3.3 Model coupling

Moreover, the continuity and momentum equations are decoupled from temperature prediction model. Consistent time step can be expressed as the following equation:

$$\Delta t = \frac{\Delta z}{v_g}. \tag{60}$$

When H_2S is released from the drilling fluid, the state changes from supercritical to gas, which directly leads to a significant increase in gas void fraction. The gasification volume of H_2S is influenced greatly by the temperature at

$$j=1 \quad T_{i,1}^{t+\Delta t}=T_{i,1}^{t}+\frac{\omega\left[\left(a_{\mathrm{NN}i1}^{t+\Delta t}T_{i-2,1}^{t+\Delta t}+a_{\mathrm{N}i1}^{t+\Delta t}T_{i-1,1}^{t+\Delta t}+a_{\mathrm{S}i1}^{t+\Delta t}T_{i+1,1}^{t+\Delta t}+a_{\mathrm{E}i1}^{t+\Delta t}T_{i,2}^{t+\Delta t}+b_{i1}^{t+\Delta t}\right)-a_{\mathrm{P}i1}^{t+\Delta t}T_{i,1}^{t}\right]}{a_{\mathrm{P}i1}^{t+\Delta t}}, \tag{56}$$

$$j=2 \quad T_{i,2}^{t+\Delta t}=T_{i,2}^{t}+\frac{\omega\left[\left(a_{\mathrm{N}i2}^{t+\Delta t}T_{i-1,2}^{t+\Delta t}+a_{\mathrm{W}i2}^{t+\Delta t}T_{i,1}^{t+\Delta t}+a_{\mathrm{S}i2}^{t+\Delta t}T_{i+1,2}^{t+\Delta t}+a_{\mathrm{E}i2}^{t+\Delta t}T_{i,3}^{t+\Delta t}+b_{i2}^{t+\Delta t}\right)-a_{\mathrm{P}i2}^{t+\Delta t}T_{i,2}^{t}\right]}{a_{\mathrm{P}i2}^{t+\Delta t}}, \tag{57}$$

$$j=3 \quad T_{i,3}^{t+\Delta t}=T_{i,3}^{t}+\frac{\omega\left[\left(a_{\mathrm{SS}i3}^{t+\Delta t}T_{i+2,3}^{t+\Delta t}+a_{\mathrm{N}i3}^{t+\Delta t}T_{i-1,3}^{t+\Delta t}+a_{\mathrm{W}i3}^{t+\Delta t}T_{i,2}^{t+\Delta t}+a_{\mathrm{S}i3}^{t+\Delta t}T_{i+1,3}^{t+\Delta t}+a_{\mathrm{E}i3}^{t+\Delta t}T_{i,4}^{t+\Delta t}+b_{i3}^{t+\Delta t}\right)-a_{\mathrm{P}i3}^{t+\Delta t}T_{i,3}^{t}\right]}{a_{\mathrm{P}i3}^{t+\Delta t}}, \tag{58}$$

$$j\geq 4 \quad T_{i,j}^{t+\Delta t}=T_{i,j}^{t}+\frac{\omega\left[\left(a_{\mathrm{N}ij}^{t+\Delta t}T_{i-1,j}^{t+\Delta t}+a_{\mathrm{W}ij}^{t+\Delta t}T_{i,j-1}^{t+\Delta t}+a_{\mathrm{S}ij}^{t+\Delta t}T_{i+1,j}^{t+\Delta t}+a_{\mathrm{E}ij}^{t+\Delta t}T_{i,j+1}^{t+\Delta t}+b_{ij}^{t+\Delta t}\right)-a_{\mathrm{P}ij}^{t+\Delta t}T_{i,j}^{t}\right]}{a_{\mathrm{P}ij}^{t+\Delta t}}. \tag{59}$$

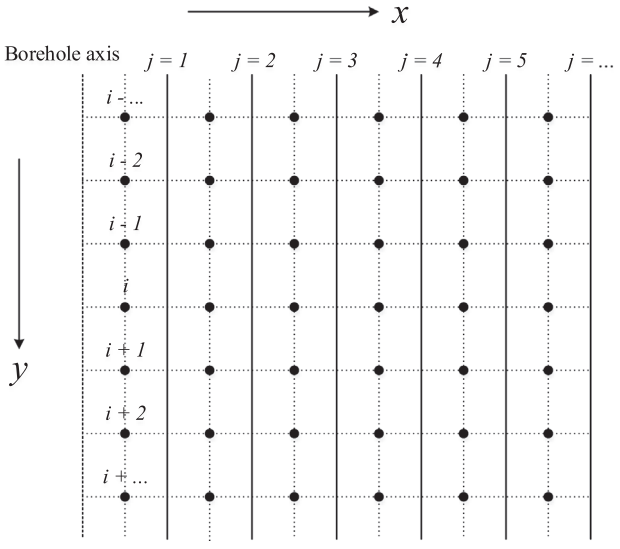

Fig. 2. The grid diagram of the wellbore and formation.

a certain well depth. And the temperature also has a significant effect on the fluid properties (Xu *et al.*, 2019). Therefore, before solving the mass and momentum equations, we must solve the transient temperature prediction model.

The well-killing simulation is based on the overflow condition at shut-in time; thus, the entire solution process can be divided into two steps: overflow and well-killing periods. For overflow period, the solution flowchart of overflow simulation is depicted in Figure 4. For well-killing period, the solution flowchart of well-killing simulation is depicted in Figure 5. As shown in the figure, depending on whether the gas reaches the wellhead, the solution process can be divided into two parts: gas rising and gas exhausting stages. The boundary positions of two-phase segment are key parameters in distinguishing the killing stage. The two-phase flow module used in the overflow period is also called

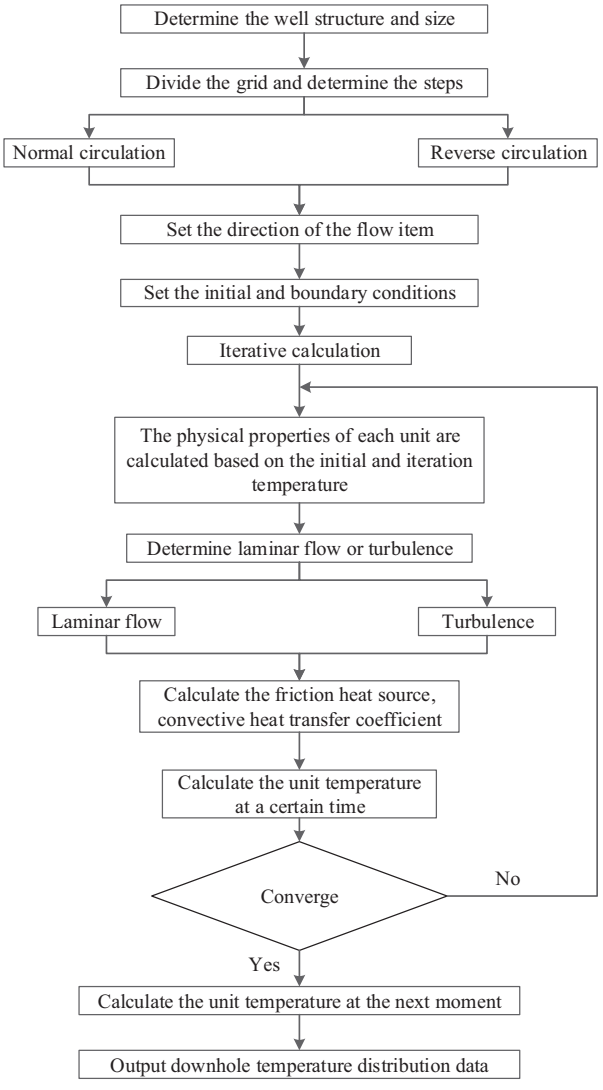

Fig. 3. Flow chart of the model solution process.

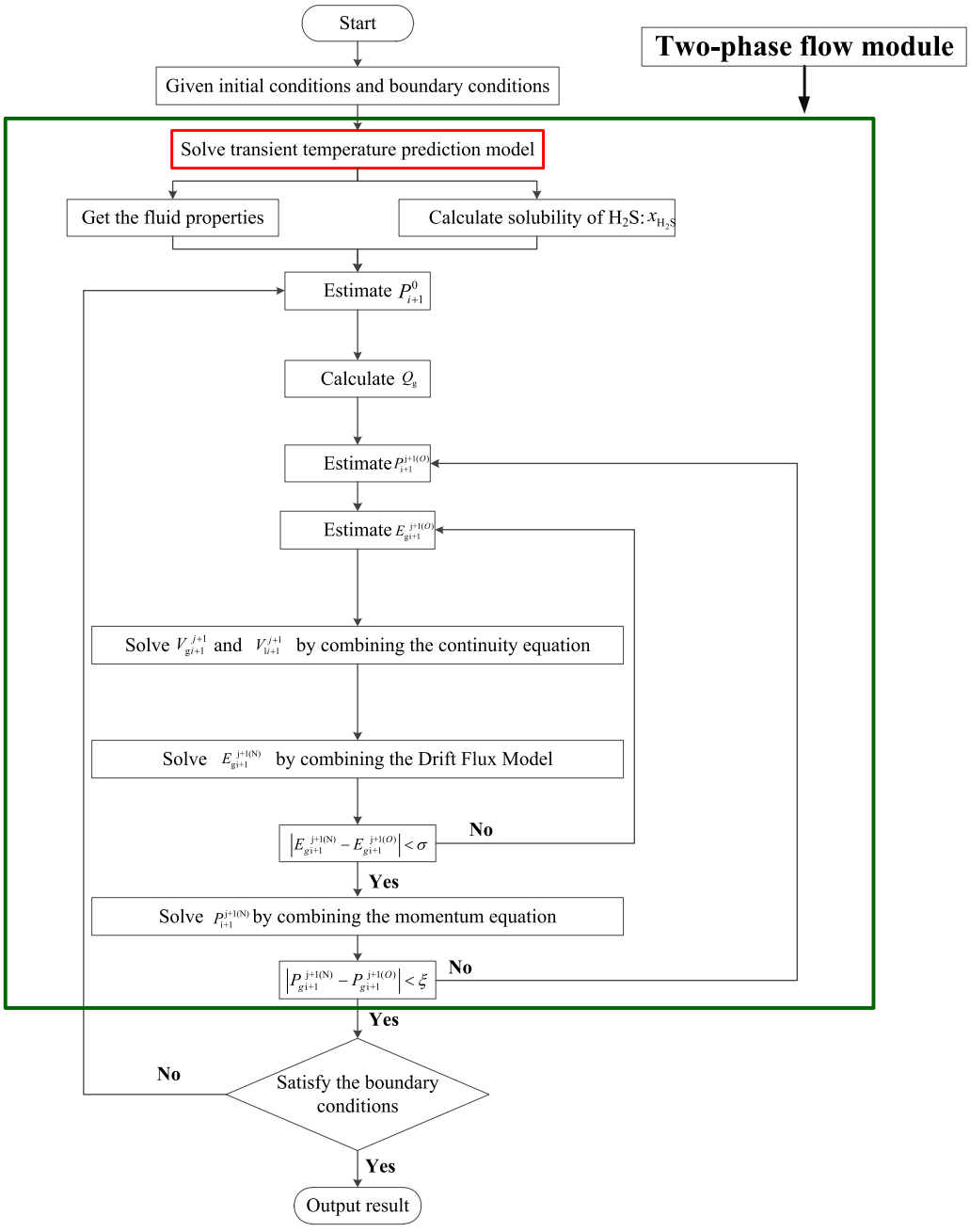

Fig. 4. Solution flowchart of overflow simulation for coupling model.

to solve the two-phase flow behavior in the well-killing period.

4 Model validation

The basic data of an H_2S-containing gas well Tiandong #5 were used to simulate the overflow process for verifying the validity of the dynamical well-killing model considering an H_2S solubility. The overflow was found in Well Tiandong #5 at the drilling depth of 3570 m, and the pit gain was 1.65 m^3 at 22:14. At 22:44, the wellhead emitted a loud noise, and a violent blowout accident occurred. The pit gain was recorded every 5 min, and the gas well was shut in when the pit gain reached 6 m^3 at 22:44. Table 1 shows the basic parameters of Well Tiandong #5 (Blowout accident of TianDong #5 well, 1990). As shown in Figure 6a, the simulation results are in good agreement with the field data of Well Tiandong #5. When H_2S is released, the pit gain shows a sudden increase in simulation results and field data. The slight difference between the two may be due to that the compressibility of the drilling fluid is disregarded.

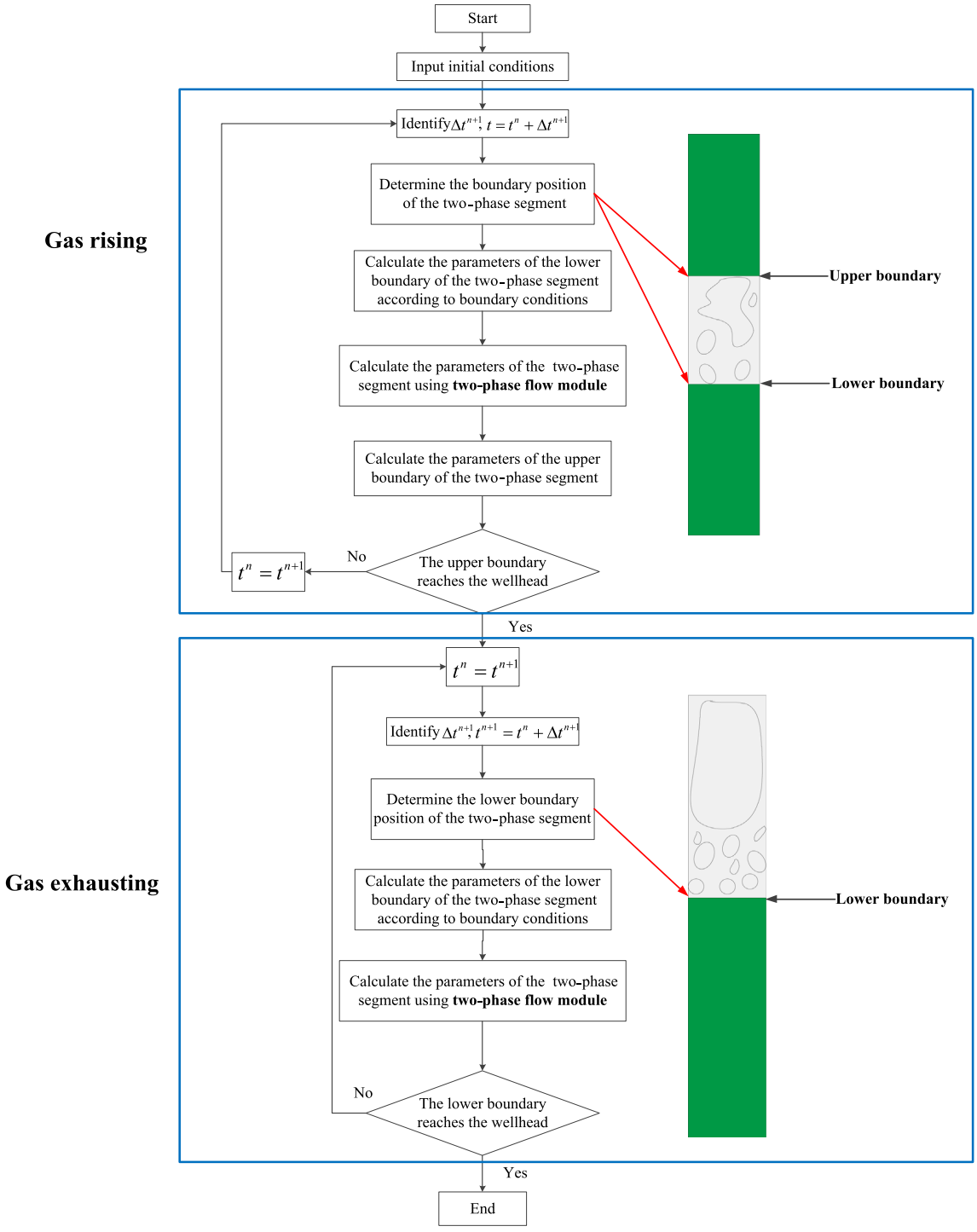

Fig. 5. Solution flowchart of well-killing simulation.

Rader conducted a gas kick and well-killing experiment in an artificial well L.S.U. 7 and provided the experimental data (Rader *et al.*, 1975). The basic data of experimental well L.S.U. 7 were used to simulate the killing process, as shown in Table 2, for validating the validity of the well-killing model. In the experiment, (1) nitrogen was injected into the well bottom hole from the injection pipe until the pit gain was 1.59 m^3, and gas was continued to inject during the shut-in operation; (2) injection of gas was stopped when the casing pressure reached the desired value; (3) well killing was started. Figure 6b shows the comparison between simulation and experimental results. As shown in Figure 6b, the simulation results of our model are in good agreement with the experimental results. The comparison between

Table 1. Basic parameters of Well Tiandong #5.

Parameter	Value	Unit
Initial gas flux	0.054	m^3/s
Drilling fluid density	1.3	g/cm^3
H_2S content	10%	
Surface temperature	10	°C
Well depth	3570	m
Drilling speed	0.05	m/s
Reservoir permeability	27	mD
Reservoir thickness	1.9	m
Plastic viscosity of drilling fluid	0.027	Pa s
Yield value of drilling fluid	1.2	Pa
Mud displacement	24	L/s
Geothermal gradient	0.026	°C/m

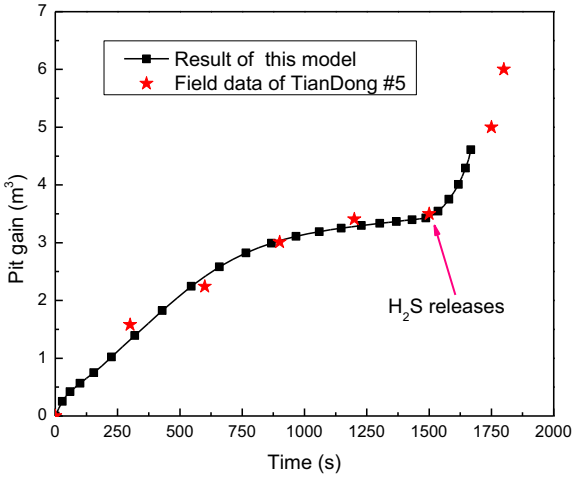

(a) Comparison between simulation and field data of Well Tiandong #5

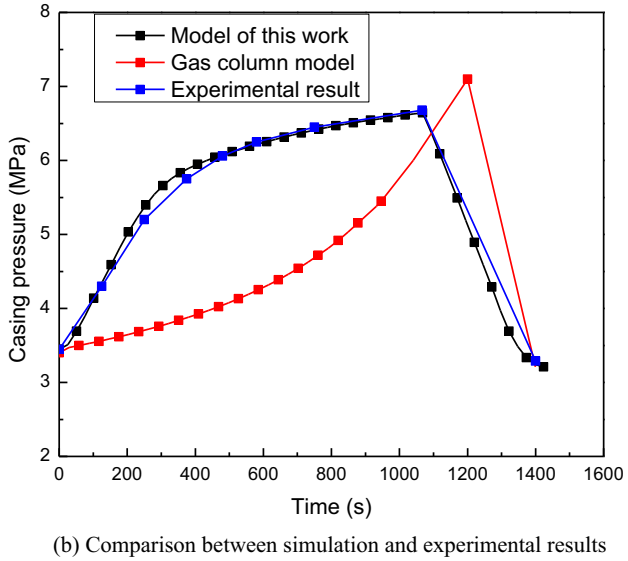

(b) Comparison between simulation and experimental results

Fig. 6. Comparison results: (a) is the comparison between simulation and field data of Well Tiandong #5; (b) is the comparison between simulation and experimental results.

Table 2. Basic data of experimental well L.S.U 7.

Parameter	Value	Unit
Inner diameter of casing	0.1243	m
Outer diameter of drilling string	0.073	m
Diameter of gas injection pipe	0.0254	m
Drilling fluid density	1.03	g/cm^3
Well depth	1832.2	m
Pumping speed of killing	60	r/min
Surface temperature	23.9	°C
Reservoir thickness	1.9	m
Plastic viscosity of drilling fluid	0.0126	Pa s
Casing pressure at shut-in time	3.447	MPa
Gas void fraction	0.75	

Table 3. Major computational parameters of the gas well in Sichuan.

Parameter	Value	Unit
Initial gas flux	0.06	m^3/s
Drilling fluid density	1.2	g/cm^3
Weighted drilling fluid	1.4	g/cm^3
H_2S content	2%	
Surface temperature	40	°C
Well depth	3000	m
Drilling speed	0.08	m/s
Reservoir permeability	40	mD
Reservoir thickness	2	m
Plastic viscosity of drilling fluid	0.03	Pa s
Yield value of drilling fluid	1.5	Pa
Mud displacement	20	L/s
Threshold value of pit gain	3	m^3
Geothermal gradient	0.024	°C/m

simulation results of our model and traditional "Gas column model" is also shown in Figure 6b. Large error exists in the simulation results of "Gas column model" because the friction and slip between gas and liquid are ignored.

5 Case study

The basic parameters from Table 3 are used to simulate the killing process of an H_2S-containing natural gas well in Sichuan. The number of spatial nodes is 60 and number of spatial nodes is 80 in the simulation. The wellbore configuration of this well is shown in Figure 7. When overflow behavior occurs, the invaded gas will push the drilling fluid with the same volume out of the wellbore, thereby leading to an increase in the pit gain. In drilling engineering, once the pit gain exceeds a threshold value, a shut-in operation must be performed. On the basis of field experience, the threshold value of pit gain is set as 3 m^3 in this work.

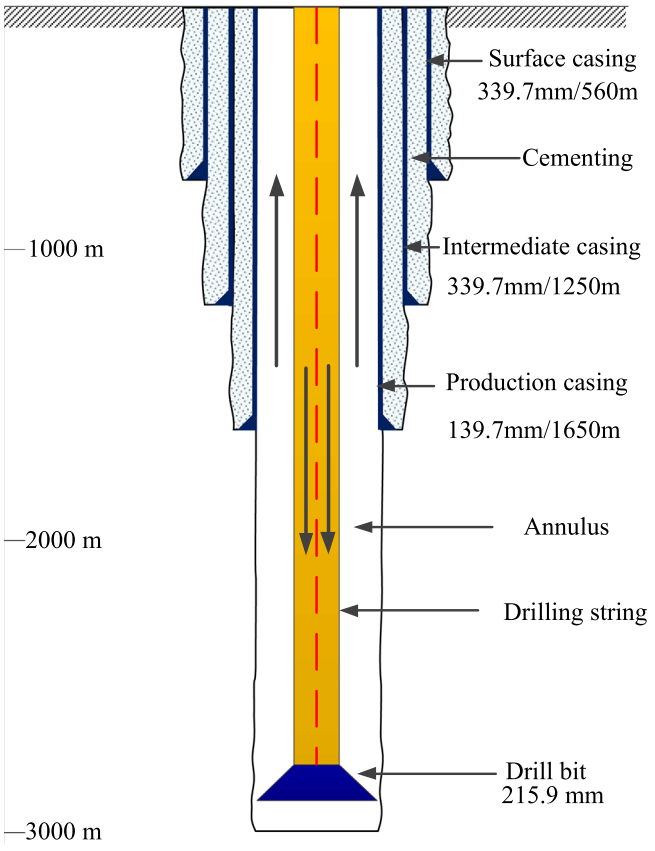

Fig. 7. Wellbore configuration of the well in Sichuan.

Figure 8a shows the change in gas void fraction and solubility of H_2S with the variation in well depth at shut-in time. As shown in the figure, gas rises to a location that is 1800 m below the wellhead, and the maximal gas void fraction is approximately 0.471. The flow pattern criterion proposed by Hasan and Kabir (1988) indicates that three flow patterns exist in the wellbore: bubble, slug, and single phase flows. Besides, the H_2S solubility decreases as the well depth decreases. This phenomenon can be attributed to the decrease in annular temperature and pressure with the well depth, as shown in Figures 8b and 8c. When the solubility of H_2S decreases to H_2S concentration in the drilling fluid at about 500 m, the phase change of H_2S occurs.

Figure 8b shows the drilling fluid temperature distribution in the drilling string and annulus at shut-in time. The annular temperature is always higher than that in the drilling string because the drilling fluid in the annulus is closer to the formation, thus, more heat can be gotten from the formation. Moreover, the annular temperature and geothermal temperature intersect at about 2250 m, which indicates that when the well depth is less than 2250 m, the drilling fluid in the annulus can be cooled by the formation. When the well depth is greater than 2250 m, the drilling fluid in the annulus can be heated by the formation. Figure 8c shows the change in annular pressure with the variation in well depth at shut-in time. As shown in Figure 8c, the annular pressure below 2000 m is lower than

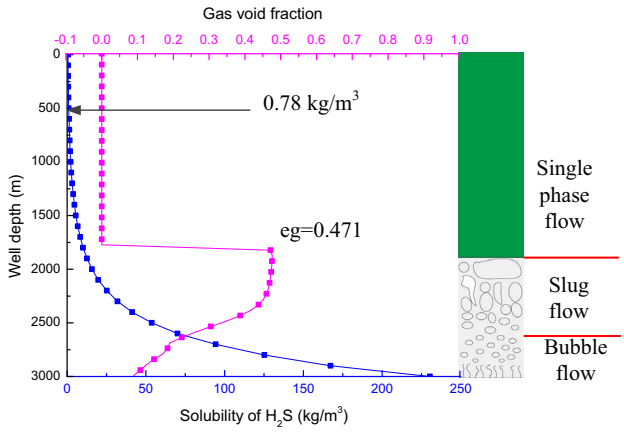

a) Gas void fraction and solubility of H_2S

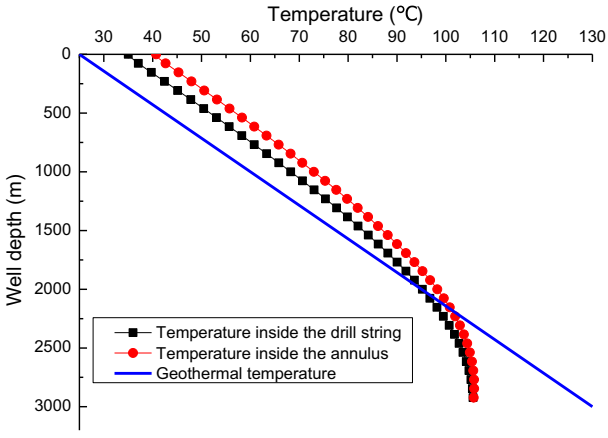

(b) Annular temperature

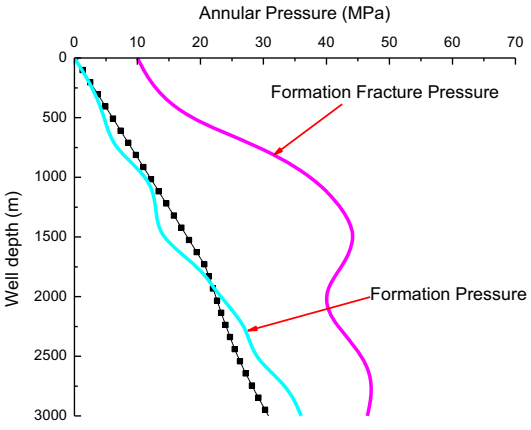

(c) Annular pressure

Fig. 8. Change in gas void fraction, solubility of H_2S, annular temperature and annular pressure with the variation in well depth at shut-in time: (a) Gas void fraction and solubility of H_2S; (b) Annular temperature; (c) Annular pressure.

the formation pressure. This phenomenon can be attributed to an invasion of natural gas, which increases the differential pressure between bottom hole and formation.

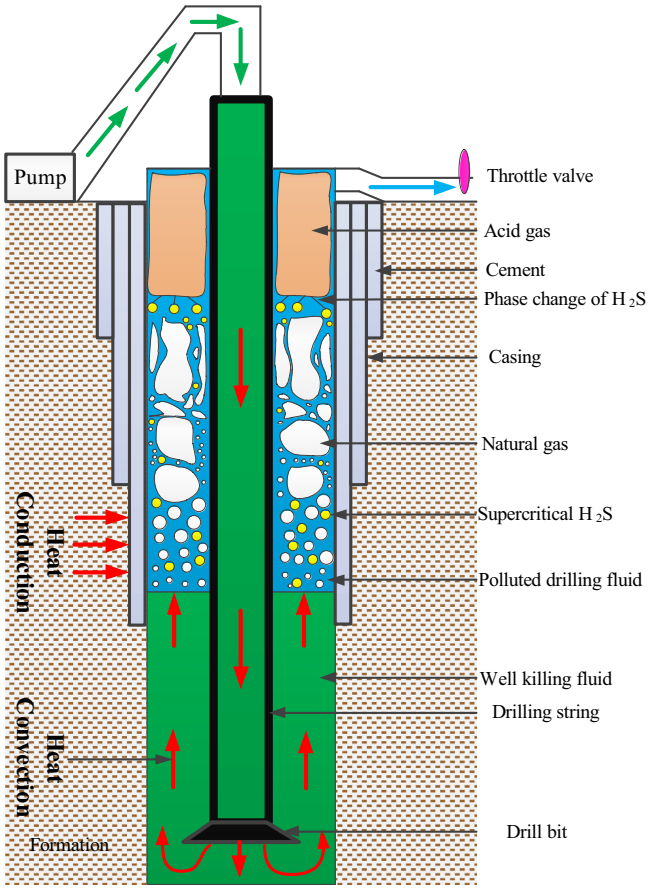

Fig. 9. Physical model of the killing process.

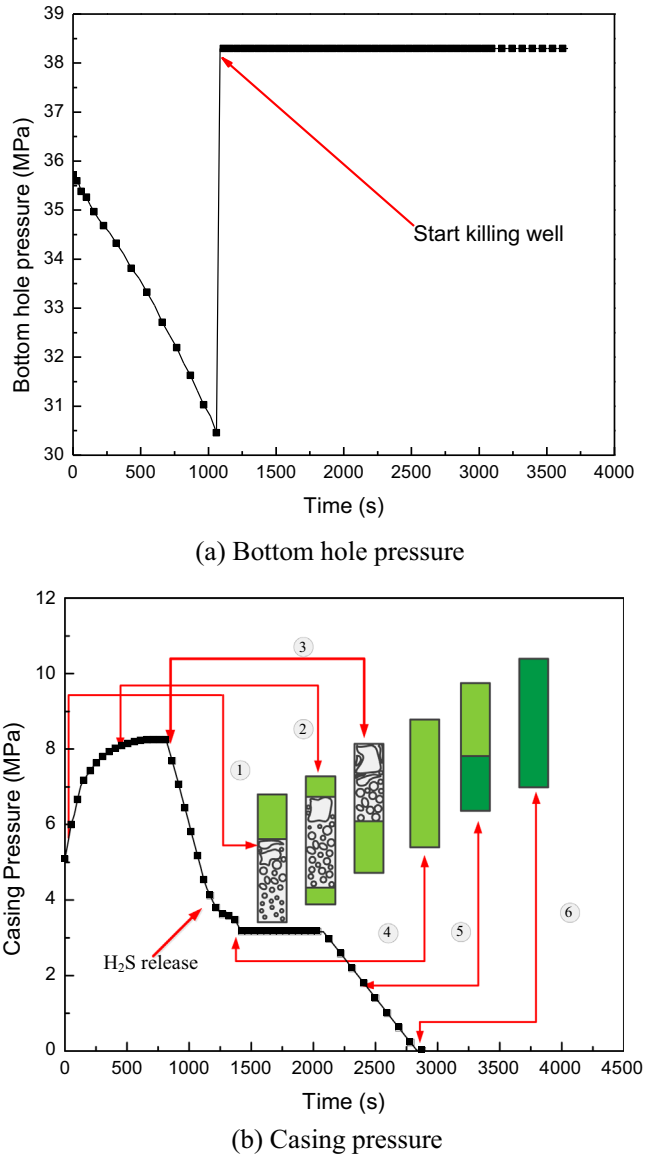

Fig. 10. Change in bottom hole pressure and casing pressure the variation in time: (a) Bottom hole pressure; (b) Casing pressure.

The increasing differential pressure will cause an increase in gas flow from formation to the wellbore and result in blow-out accidents easily if not controlled.

Driller's method is widely used in well killing in oil and gas fields (Feng *et al.*, 2016a). Thus, the method is also used in the simulation of this work. Figure 9 shows the physical model of the killing process. During killing, the pressure balance relationship can be expressed as follows (Feng *et al.*, 2016b):

$$P_{\mathrm{p}} \leq P_{\mathrm{b}} = P_{\mathrm{a}} + P_{\mathrm{la}} + P_{\mathrm{ma}}. \tag{61}$$

Figure 10a shows the change in bottom hole pressure with the variation in time. As shown in the figure, the bottom hole pressure first decreases during the overflow period and then keeps constant (greater or equal to formation pressure) when well killing is conducted. Therefore, no gas flows into the wellbore from the formation during killing.

With the change in hydrostatic pressure created by the fluid column, the casing pressure of the wellhead can be changed by adjusting the throttle opening to maintain the bottom hole pressure constant. Figure 10b shows the change in casing pressure with the variation in time. As shown in the figure, the entire killing process can be divided into six stages. Stage 1 is the initial stage of the killing process, which is determined by the flow pattern at shut-in time. Stage 2 indicates that the two-phase section in the wellbore is rising up toward the wellbore prior to reaching the wellhead. At this time, the flow pattern distribution in the wellbore is single phase flow, gas–liquid two-phase flow, and single phase flow in sequence. Moreover, the casing pressure increases with the increase in killing time. This phenomenon is attributed to the slippage and expansion of gas. The gas will expand as it rises up along the wellbore because the annular and formation temperatures and depth decrease (Sun *et al.*, 2018). Thus, the hydrostatic pressure decreases accordingly and the casing pressure increases to keep the bottom hole pressure constant. Stage 3 indicates that the gas reaches the wellhead and single phase and gas–liquid two-phase flows exist in the wellbore. The total gas volume reaches a maximum at this point.

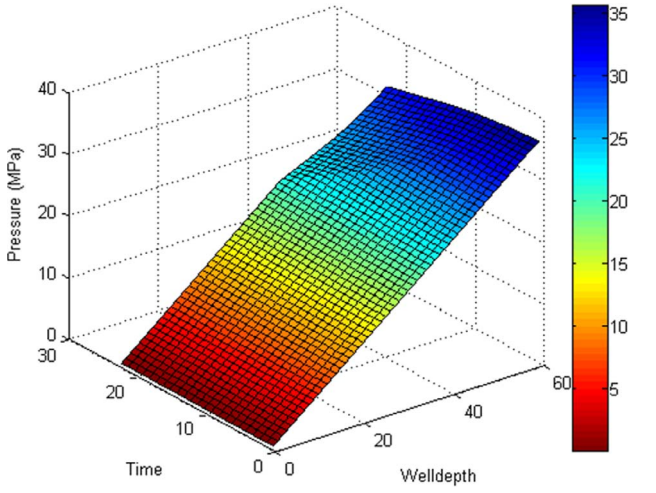

a) Gas kick

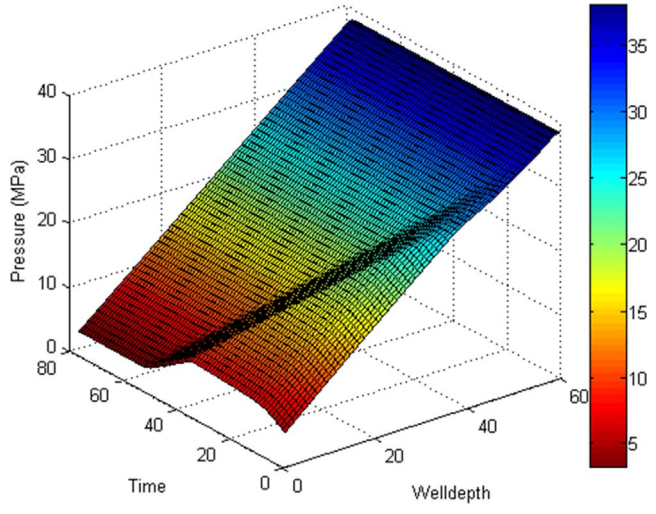

(b) Well killing

Fig. 11. Dynamical pressure distribution in the wellbore: (a) during gas kick; (b) during well killing.

Stage 4 indicates that all the gas has been pushed out of the wellbore and only single phase flow exists in the wellbore. This stage will last for some time until the weighted drilling fluid enters the annulus. Furthermore, the casing pressure keeps constant in Stage 4. Stage 5 indicates that the weighted drilling fluid enters the annulus and the hydrostatic pressure increases. Thus, the casing pressure decreases. Stage 6 indicates that the annulus is full of the weighted drilling fluid and the casing pressure decreases to 0. The well-killing operation ends.

Figure 10b also shows that, when all the gas is about to be pushed out of the well, H_2S is released, and the curve drops slowly. This phenomenon is the result of casing pressure applied at the wellhead. Figure 8a shows that, when overflow behavior occurs, H_2S will release at a location close to the wellhead if shut-in operation is not performed. However, H_2S solubility decreases with the increase in pressure, and the casing pressure applied at the wellhead changes the pressure distribution in the wellbore (Fig. 11). As shown in Figure 11, the pressure of each location along the wellbore is higher than that of the overflow process during the killing process. Therefore, the H_2S solubility of each location in the killing process increases compared with that of shut-in time. Although it reaches the wellhead, the H_2S will not release until the H_2S solubility is lower than its content in the drilling fluid. Therefore, when the casing pressure decreases, the H_2S solubility decreases. As a result, the H_2S transforms from a supercritical phase to a gas phase, gas volume expands suddenly, and gas void fraction increases abruptly. Thus, the casing pressure drops slowly.

5.1 Analysis under different H_2S contents

Considering that the phase change of H_2S occurs at low pressure and temperature and the phase change of H_2S has a great effect on the pressure distribution (Sun *et al.*, 2013), the diagrams of wellhead flow pattern when gas reaches wellhead during well killing under different working conditions are depicted to study the flows at wellhead.

Figure 12 shows the diagram of wellhead flow pattern when gas reaches wellhead during well killing with H_2S contents of 0%, 2%, 4%, and 6%. As shown in the figure, the gas void fraction increases with the increase in H_2S content. This phenomenon is caused by the increase in gasification volume of H_2S as H_2S content increases. When the well depth decreases, the annular pressure and annular temperature decrease, as shown in Figure 13. Besides, the higher the H_2S content is, the lower the annular temperature will be as shown in Figure 13b. This is because, near the critical point of H_2S, the viscosity of supercritical H_2S decreases significantly (Vesovic *et al.*, 1998). Therefore, in the upper well section, the convective heat transfer coefficient between the drilling fluid and the formation increases as viscosity of supercritical H_2S decreases. Thus, more heat will be diffused from the drilling fluid in the annulus to the formation. As H_2S content increases, this effect will be enhanced. Therefore, in the upper well section which is near the critical point of H_2S, the annular temperature is lower at higher H_2S content and, as a result, at the same well depth, the H_2S solubility will be lower and more H_2S will gasify.

Additional H_2S will gasify at higher H_2S content, and this condition changes the wellhead flow pattern. Churn flow appears at the wellhead with H_2S content of 0%; however, when H_2S is released, annular flow appears and the droplets in the bubble decrease as H_2S content increases. Therefore, the hydrostatic pressure decreases with the increase in H_2S content, and the casing pressure increases to keep the bottom hole pressure constant. Figure 14 shows that, when H_2S is released, the casing pressure increases with H_2S content. Thus, the annular pressure of the upper well section increases with the increase in H_2S content, as shown in Figure 13a. However, H_2S content has a small effect on entire wellbore pressure distribution, as shown in Figure 14.

From comparison between Figures 8c and 13a, it can be concluded that well killing can rebuild the pressure distribution in the wellbore and stop the overflow behavior caused by the pressure differential between bottom hole and formation. However, for the stratum with low formation fracture

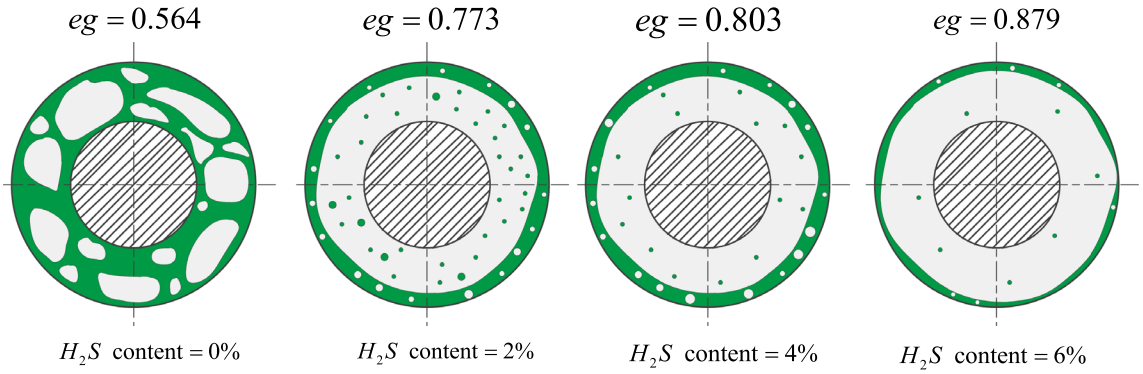

Fig. 12. Diagram of wellhead flow pattern when gas reaches wellhead during well killing with H_2S contents of 0%, 2%, 4%, and 6%.

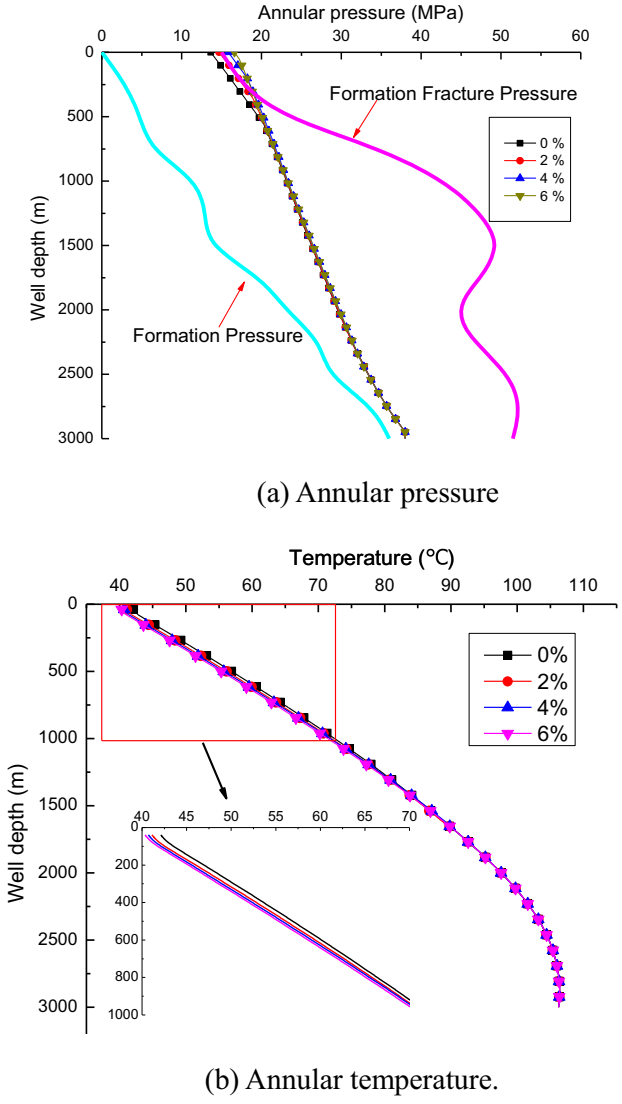

Fig. 13. Change in annular pressure and temperature with the variation in well depth at 1300 s during well killing with H_2S contents of 0%, 2%, 4%, and 6%: (a) Annular pressure; (b) Annular temperature.

pressure, the well-killing operation may cause annulus pressure to approach or exceed formation fracture pressure, thereby causing well leakage. This scenario should be highly regarded, especially for H_2S-containing natural gas wells. Figure 13a shows that, when H_2S is released, the annular pressure of the upper well section will exceed the formation fracture pressure. Moreover, a high H_2S content indicates serious fracture of the stratum. Therefore, during the late period of well killing in H_2S-containing natural gas wells, the casing pressure should be reduced appropriately to avoid stratum fracturing and prevent leakage accidents.

5.2 Analysis under different initial overflow volumes

Figure 15 shows the diagram of wellhead flow pattern when gas reaches wellhead during well killing with initial overflow volumes of 2, 4, and 8 m^3. As shown in the figure, the gas void fraction increases with the increase in initial overflow volume because a large amount of gas enters the wellbore at high initial overflow volume. Moreover, the wellhead flow pattern with initial overflow volume of 2 m^3 can be regarded as slug flow, whereas the annular flow appears at high initial overflow volumes of 4 and 8 m^3. The gas phase becomes continuous at initial overflow volumes of 4 and 8 m^3. The continuous phase volume increases as the initial overflow volume increases.

A high initial overflow volume indicates gas rises to a high location in the wellbore at shut-in time. When initial overflow volume reaches 8 m^3, the gas enters the wellhead at shut-in time. This conclusion can also be drawn from Figure 16. Figure 16b shows the change in casing pressure with the variation in time and initial overflow volumes of 2, 4, and 8 m^3. As shown in the figure, the surface casing pressure increases with the increase in initial overflow volume. This phenomenon can be attributed to the increase in hydrostatic pressure loss as gas volume increases. Thus, additional surface casing pressure should be applied to balance the bottom hole pressure at high initial overflow volume. Moreover, as shown in Figure 16b, the pressure change in the wellbore intensifies as initial overflow volume increases.

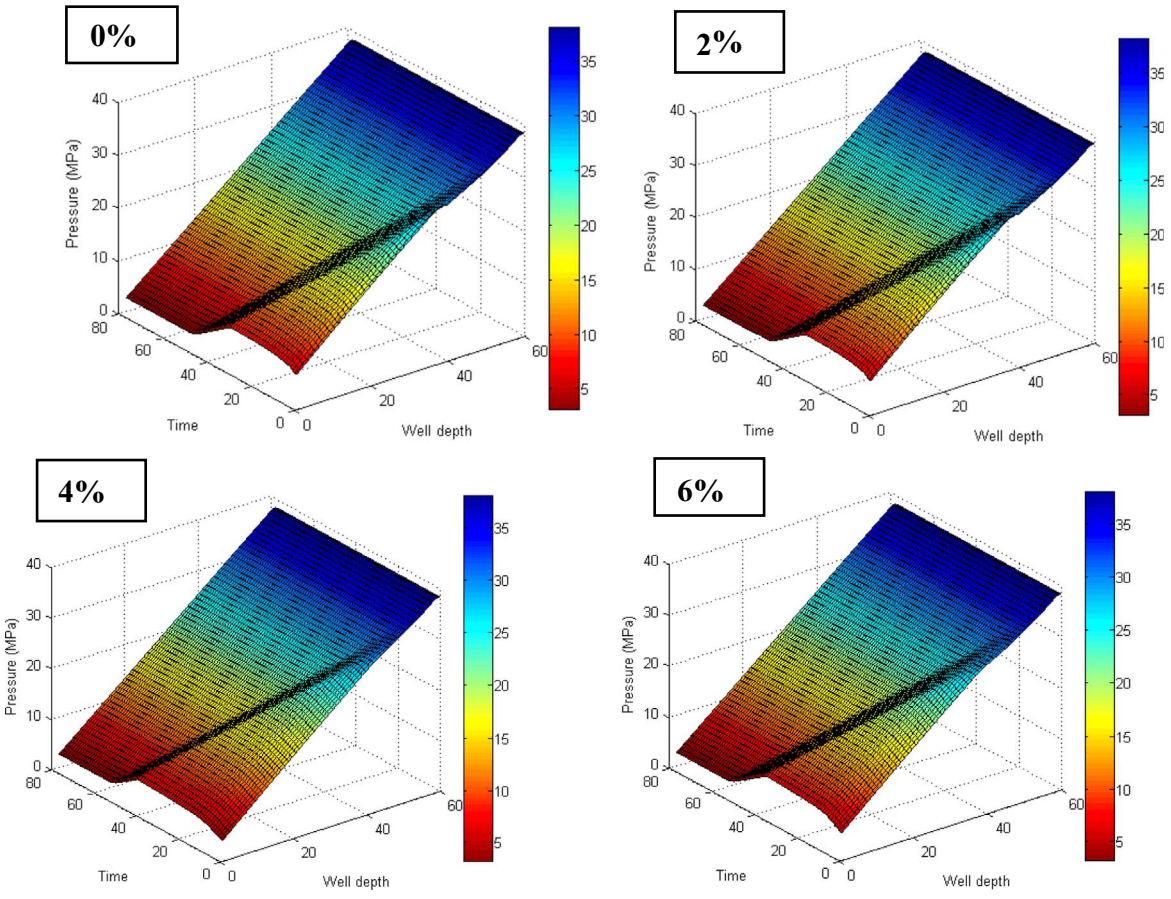

(a) Wellbore pressure

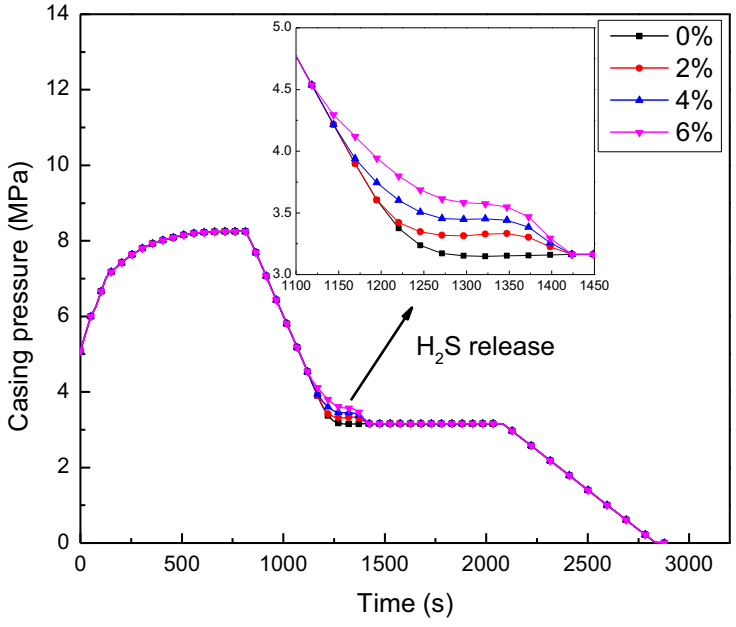

(b) Casing pressure

Fig. 14. Change in wellbore pressure and casing pressure with the variation in time and H_2S contents of 0%, 2%, 4%, and 6%:

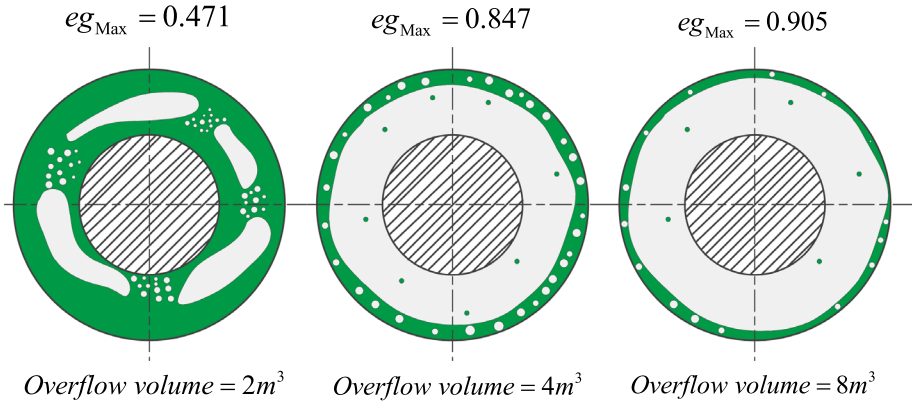

Fig. 15. Diagram of wellhead flow pattern when gas reaches wellhead during well killing with initial overflow volumes of 2, 4, and 8 m^3.

Besides, as the initial overflow volume increases, the gasification starting time of H_2S increases and, the casing pressure is lower as shown in Figure 16a. This phenomenon can be attributed to the change of drilling fluid temperature. Figure 17a shows the change in annular temperature with the variation in well depth at 1300 s during well killing with different initial overflow volume. We can see that, the drilling fluid temperature is higher at higher initial overflow volume. This is because, as more gas enters the wellbore, more heat from the formation will be carried into the wellbore. Thus, the H_2S solubility will be higher at the same well depth and less H_2S will gasify. Therefore, when H_2S gasifies, the casing pressure applied at wellhead is higher at lower initial overflow volume.

Figure 17b shows the change in annular pressure with the variation in well depth and initial overflow volumes of 2, 4, and 8 m^3. As initial overflow volume increases, the gas expansion capacity is limited. Thus, pressure changed rapidly from 2 m^3 to 4 m^3, but slowly from 4 m^3 to 8 m^3. As shown in the figure, the annular pressure is high with high initial overflow volume. This phenomenon is caused by the increase in surface casing pressure as initial overflow volume increases. However, when initial overflow volume increases, the annular pressure may approach or even exceed the formation fracture pressure, which may lead to formation fracturing. Therefore, careful monitoring of the pit gain is necessary during the exploitation of H_2S-containing natural gas wells. Once the pit gain exceeds a threshold value, the shut-in operation should be performed immediately to prevent further overflow. Furthermore, during the late period of well killing in H_2S-containing natural gas wells with high initial overflow volume, the surface casing pressure should be decreased appropriately to avoid stratum fracturing and prevent leakage accidents. Early detection of gas kick should be more frequent to avoid severe overflow.

5.3 Analysis under different drilling fluid densities

Figure 18 shows the diagram of wellhead flow pattern when gas reaches wellhead during well killing with drilling fluid densities of 1.20, 1.25, and 1.30 g/cm^3. As shown in the figure, the gas void fraction at wellhead increases with the increase in drilling fluid density. This phenomenon can be attributed to the decrease in casing pressure caused by the increase in drilling fluid density. The annular pressure is low at shut-in time with low drilling fluid density because the hydrostatic pressure is proportional to drilling fluid density. Therefore, to maintain the bottom hole pressure, the surface casing pressure should be higher at low drilling fluid density, as shown in Figure 19. During well killing, the annular pressure is high at low drilling fluid density, as shown in Figure 20a. The gas void fraction is high at high drilling fluid density because the gas expands violently at low pressure. Figure 18 shows that the drilling fluid density slightly affects the wellhead flow pattern, and annular flow is the common flow pattern under drilling fluid densities of 1.20, 1.25, and 1.30 g/m^3.

Figure 20b shows the change in annular temperature with the variation in well depth at 1300 s during well killing with different drilling fluid density. As shown in Figure 20b, for the deeper well section, the drilling fluid temperature increases with the decrease in drilling fluid density. This is because, when the same heat is obtained from the formation, the greater the drilling fluid density, the less the increase in temperature (Gao *et al.*, 2017). For the upper well section, the drilling fluid temperature is closer to the formation temperature, the temperature differences decrease. Considering that H_2S only gasifies in the upper well section, the effect of temperature difference caused by the change in drilling fluid density on gasification of H_2S is small as shown in Figure 19b.

Furthermore, annular pressure of the upper well section will exceed the formation fracture pressure, and low drilling fluid density indicates serious fracture of the stratum. Thus, during the well killing in H_2S-containing natural gas wells, higher drilling fluid density should be used to avoid stratum fracturing and prevent leakage accidents.

5.4 Analysis under different well-killing displacements

Figure 21 shows the diagram of wellhead flow pattern when gas reaches wellhead during well killing with displacements

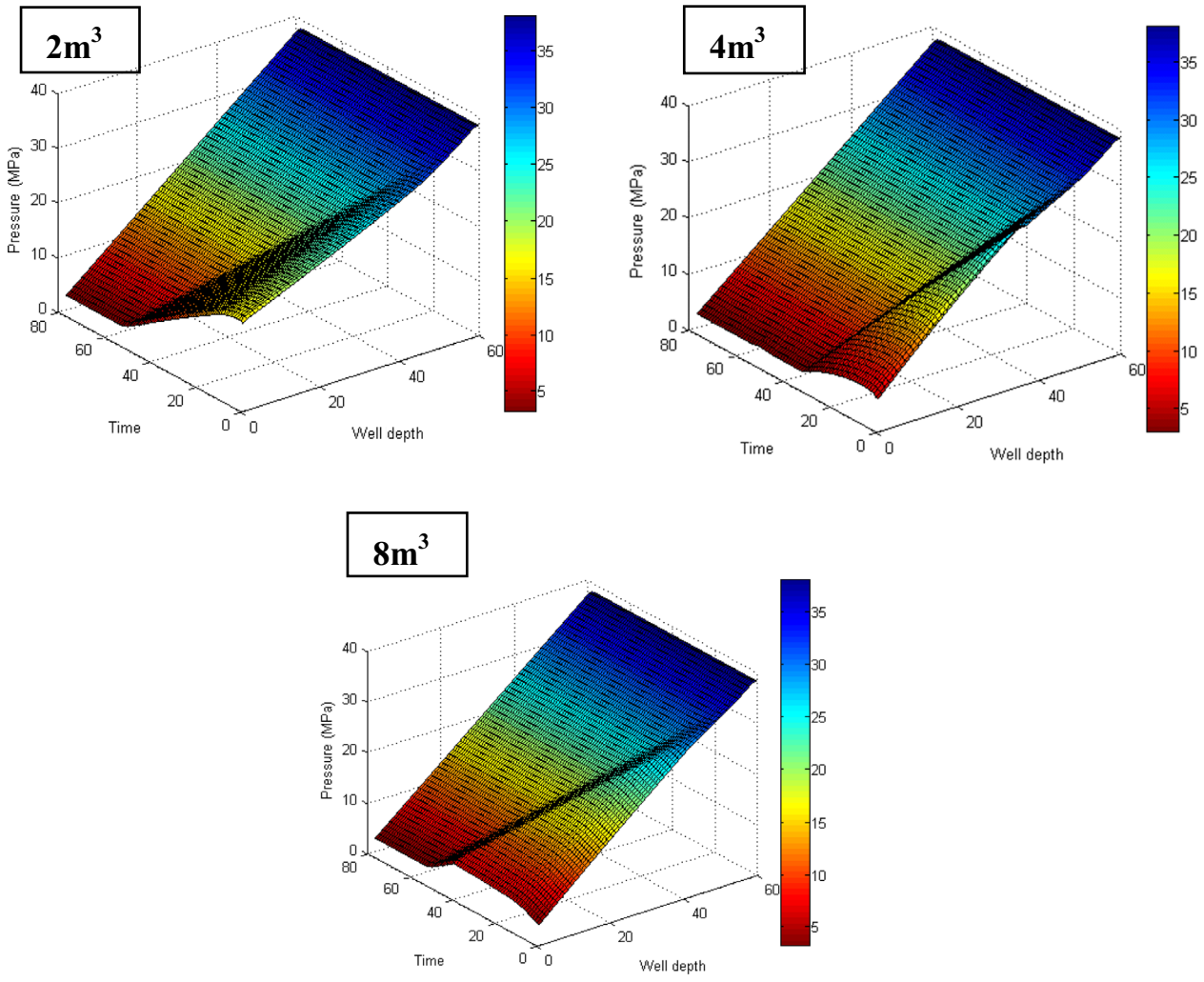

(a) Wellbore pressure

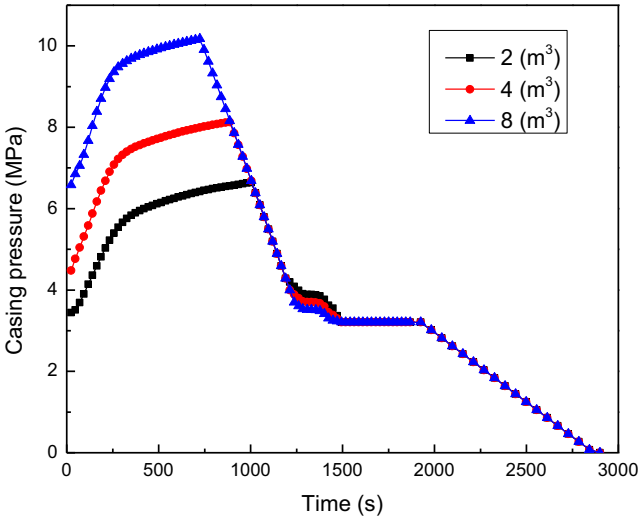

(b) Casing pressure

Fig. 16. Change in wellbore pressure and casing pressure with the variation in time and initial overflow volumes of 2, 4, and 8 m^3: (a) Wellbore pressure; (b) Casing pressure.

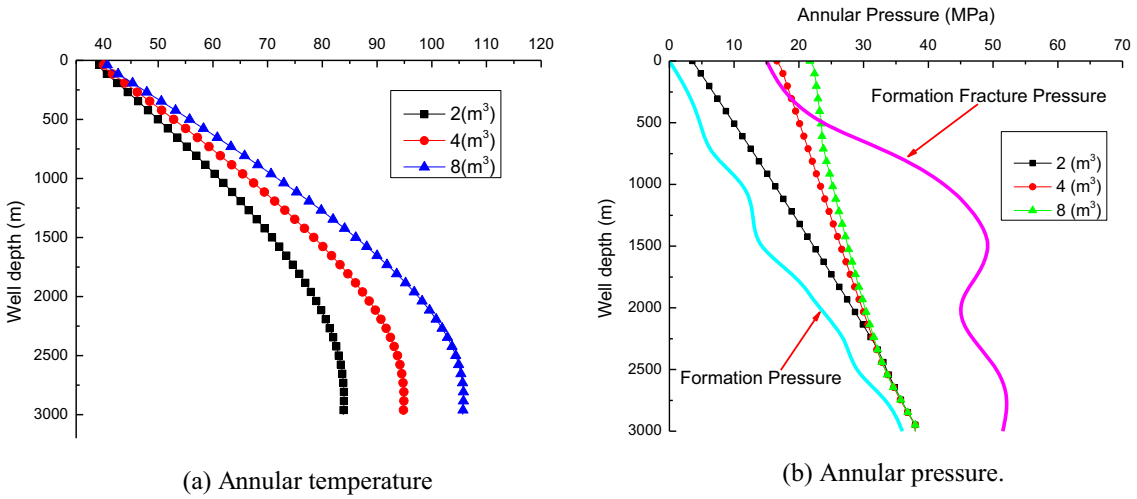

Fig. 17. Change in annular temperature and annular pressure with the variation in well depth at 1300 s during well killing with initial overflow volumes of 2, 4, and 8 m^3: (a) Annular temperature; (b) Annular pressure.

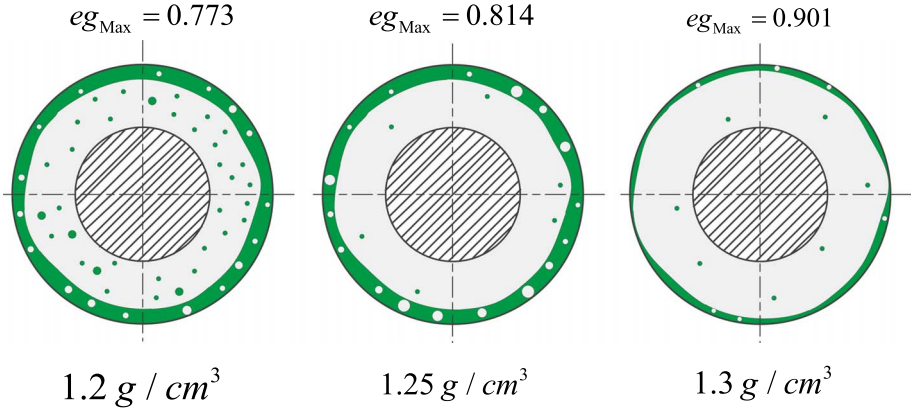

Fig. 18. Diagram of wellhead flow pattern when gas reaches wellhead during well killing with drilling fluid densities of 1.20, 1.25, and 1.30 g/cm^3.

of 20, 30, and 40 L/s. As shown in the figure, the gas void fraction at wellhead increases slightly with the increase in displacement. The annular flow is the common wellhead flow pattern under displacements of 20, 30, and 40 L/s, and the number of droplets in the continuous gas decreases with the increase in displacement.

Figure 22a shows the change in annular temperature with the variation in well depth at 1300 s during well killing with different displacement. The lower the displacement is, the longer time for heat exchange with the formation will be. Thus, for the upper well section, the annular temperature is higher than formation, at higher displacement, the drilling fluid temperature is higher because lesser heat of drilling fluid will loss. For the deeper well section, the annular temperature is lower than formation, at higher displacement, the drilling fluid temperature is lower because lesser heat from formation will be exchanged to the drilling fluid. However, the effect of displacement on temperature distribution in annulus is small.

Figure 23 shows the change in wellbore pressure and casing pressure with the variation in time and displacements of 20, 30, and 40 L/s. As shown in the figure, the higher the displacement is, the faster the gas kick leaves wellbore and, the lower the casing pressure will be. Besides, H_2S will gasify at an earlier time. This phenomenon can be attributed to the increased friction resistance due to the increase in displacement (Shi *et al.*, 2014). Thus, the bottom hole pressure increases as displacement increases and, the casing pressure decreases as a result. Therefore, the annular pressure is lower at higher displacement in the upper well section as shown in Figure 22b. Besides, the annular pressure of the upper well section will exceed the formation fracture pressure, and low displacement indicates serious fracture of the stratum. Thus, during well

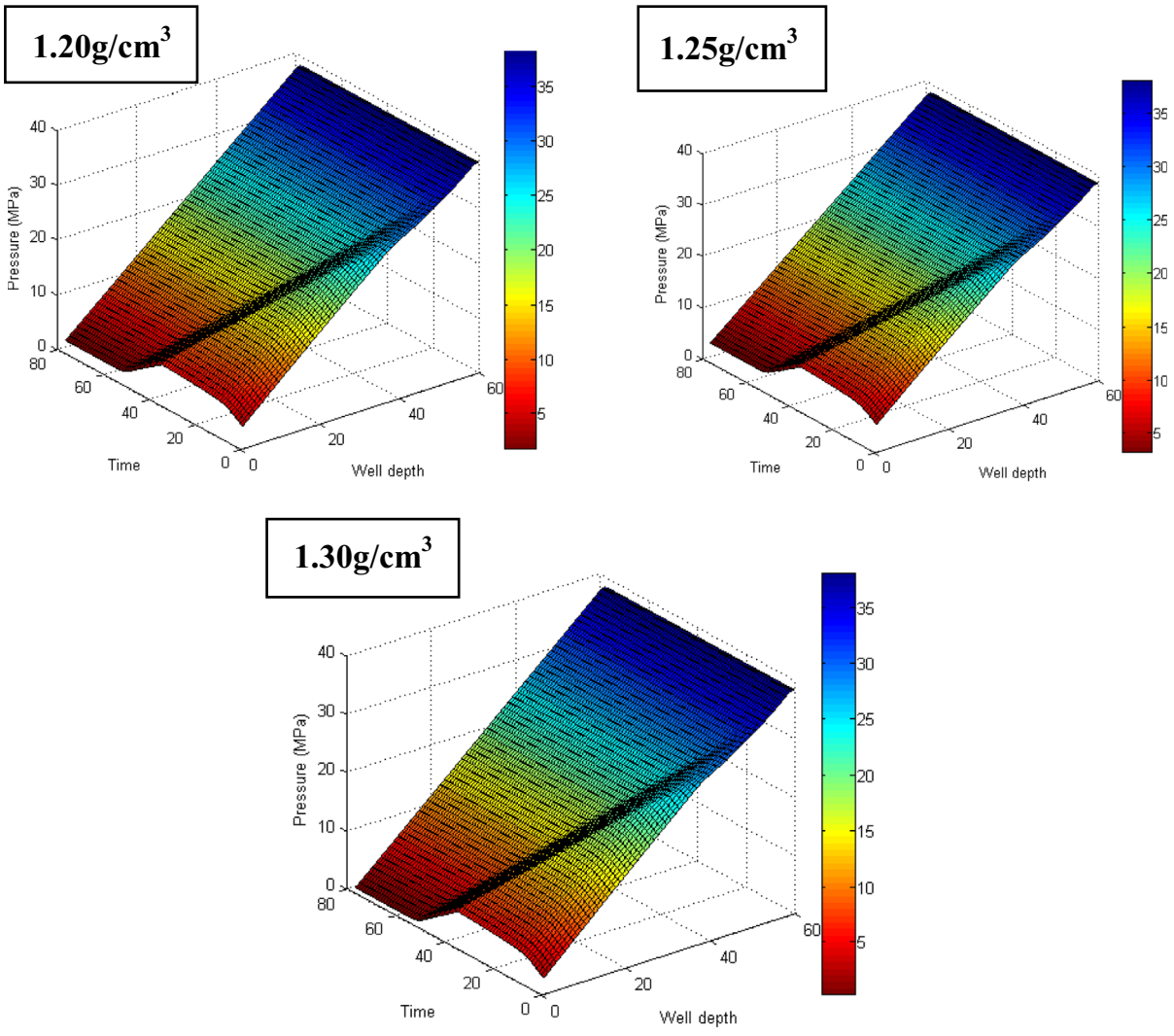

(a) Wellbore pressure

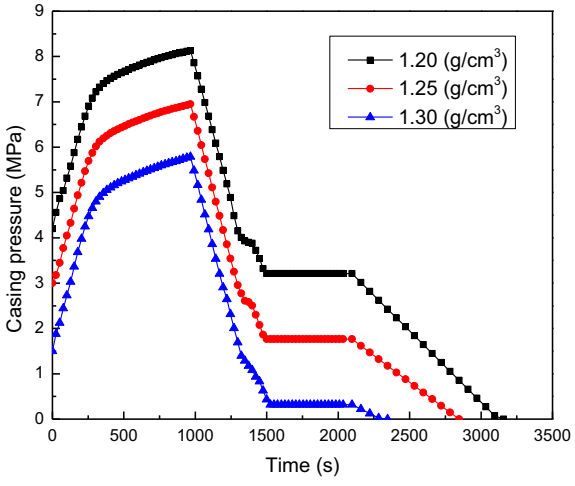

(b) Casing pressure

Fig. 19. Change in wellbore pressure and casing pressure with the variation in time and drilling fluid densities of 1.20, 1.25, and 1.30 g/cm^3: (a) Wellbore pressure; (b) Casing pressure.

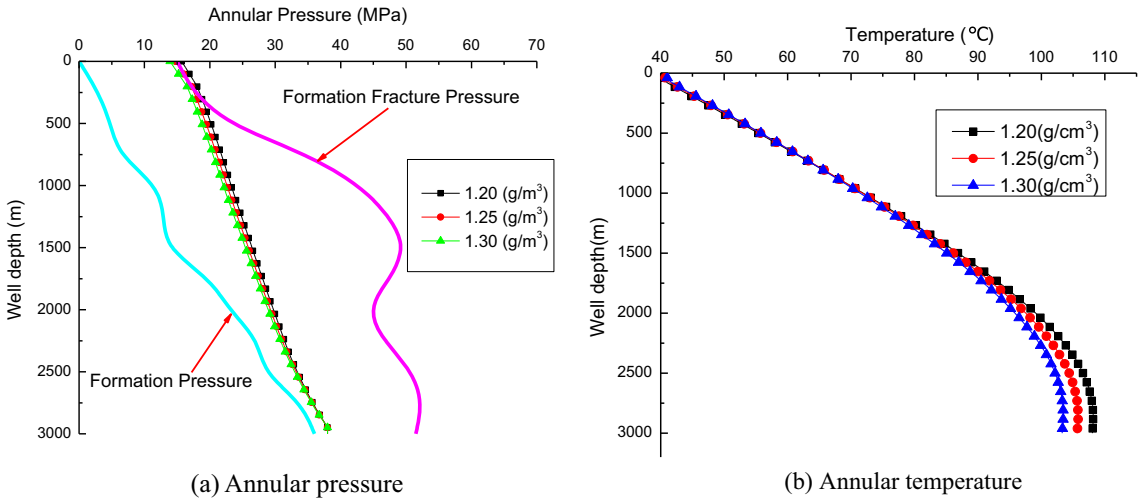

Fig. 20. Change in annular temperature and annular pressure with the variation in well depth at 1300 s during well killing with drilling fluid densities of 1.20, 1.25, and 1.30 g/cm^3: (a) Annular pressure; (b) Annular temperature.

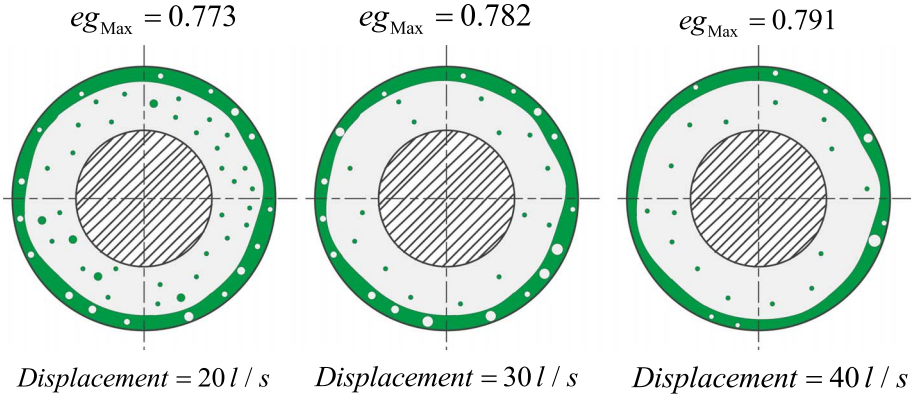

Fig. 21. Diagram of wellhead flow pattern when gas reaches wellhead during well killing with displacements of 20, 30, and 40 L/s.

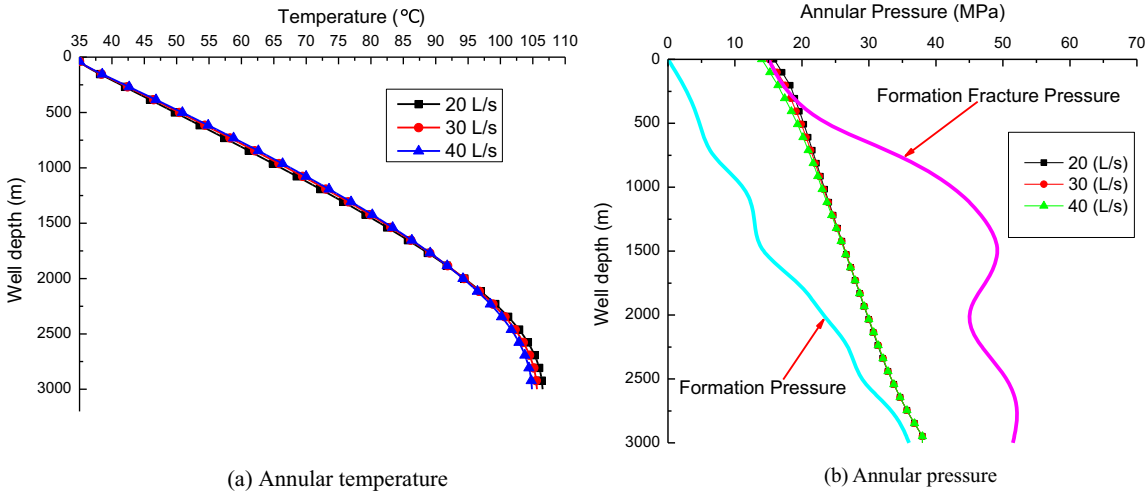

Fig. 22. Change in annular temperature and annular pressure with the variation in well depth at 1300 s during well killing with displacements of 20, 30, and 40 L/s: (a) Annular temperature; (b) Annular pressure.

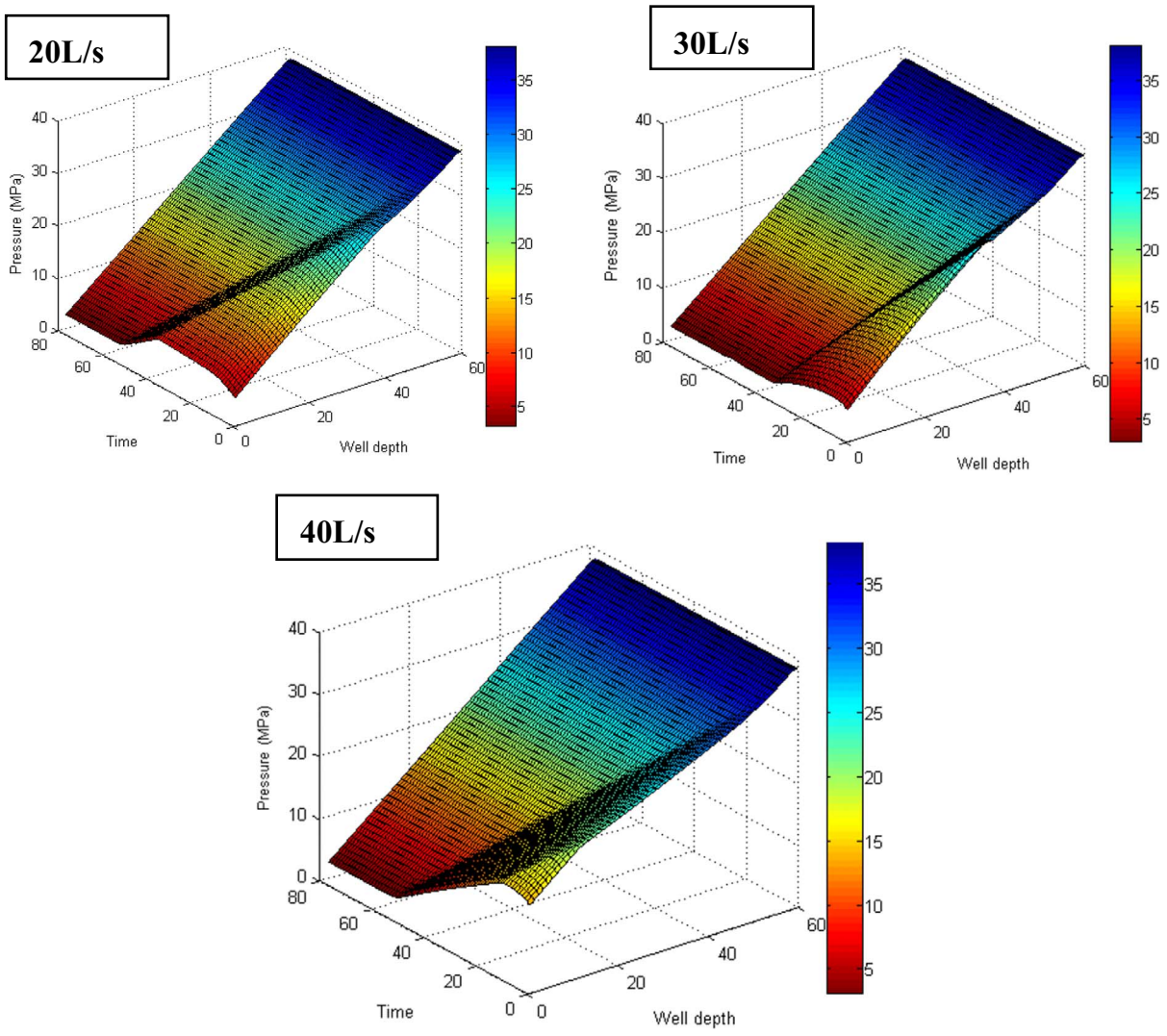

(a) Wellbore pressure

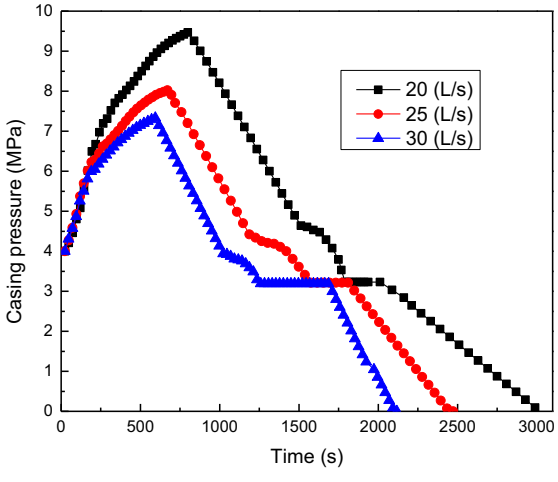

(b) Casing pressure

Fig. 23. Change in wellbore pressure and casing pressure with the variation in time with displacements of 20, 30, and 40 L/s: (a) Wellbore pressure; (b) Casing pressure.

killing in H_2S-containing natural gas wells, higher well-killing displacement should be used to avoid stratum fracturing and prevent leakage accidents.

6 Conclusion

This work established a dynamical well-killing model considering an H_2S solubility to simulate the well-killing process of a vertical H_2S-containing natural gas well. The following important conclusions can be drawn:

1. H_2S will gasify near wellhead during well killing when casing pressure decreases. Near the critical point of H_2S, the annular temperature decreases as H_2S content increases and, the H_2S solubility will be lower and more H_2S will gasify. To balance the bottom hole pressure, when H_2S releases, the casing pressure increases as H_2S content increase.
2. As initial overflow volume increases, the annular temperature, annular pressure and the casing pressure increase significantly. When H_2S gasifies, the casing pressure applied at wellhead should be higher at lower initial overflow volume to balance bottom hole pressure.
3. In the well-killing process, the annular pressure and temperature decrease as drilling fluid density increases and a lower casing pressure is needed for balancing bottom hole pressure. No significant effect of drilling fluid density on the gasification of H_2S is found. As well-killing displacement increases, for the upper well section, the annular temperature increases while the annular pressure decreases. The casing pressure is lower at a higher displacement for higher friction resistance. Besides, H_2S will gasify at an earlier time.
4. When drilling for H_2S-containing natural gas well, early detection of gas kick should be more frequent to avoid severe overflow. Besides, during well killing, higher displacement and density of drilling fluid should be considered to avoid stratum fracturing and prevent leakage accidents under the premise of meeting drilling requirements.

Acknowledgments. This work was supported by the National Key Research and Development Program of China (2019YFC0312303) and Sichuan Science and Technology Project (2019YFS0045).

References

Amaya-Gómez R., López J., Pineda H., Urbano-Caguasango D., Pinilla J., Ratkovich N., Muñoz F. (2019) Probabilistic approach of a flow pattern map for horizontal, vertical, and inclined pipes, *Oil Gas Sci. Technol. - Rev. IFP Energies nouvelles* **74**, 67.

Ansari A.M., Sylvester N.D., Sarica C., Shoham O., Brill J.P. (1994) A comprehensive mechanistic model for upward two phase flow in wellbores, *SPE Prod. Facil.* **5**, 143–152. https://doi.org/10.2523/20630-MS.

Bilicki Z., Kestin J. (1987) Transition criteria for two-phase flow patterns in vertical upward flow, *Int. J. Multiphase Flow.* **13**, 3, 283–294.

Blowout accident of TianDong well #5 (1990) *Petrochina Southwest Oil and Gas field Company.*

Ebrahimi A., Khamehchi E. (2015) A robust model for computing pressure drop in vertical multiphase flow, *J. Nat. Gas. Sci. Eng.* **26**, 1306–1316.

Elsharkawy A.M. (2004) Efficient methods for calculations of compressibility, density and viscosity of natural gases, *Fluid Phase Equilibr.* **218**, 1, 1–13.

Feng J., Fu J., Chen P., Liu Z., Wei H. (2015) Predicting pressure behavior during dynamic kill drilling with a two-phase flow, *J. Nat. Gas Sci. Eng.* **22**, 591–597.

Feng J., Fu J., Chen P., Luo J., Kou B. (2016a) Comparisons of the Driller's method and the wait and weight method in deepwater well killing operation, *Arab. J. Sci. Eng.* **41**, 7, 2699–2706.

Feng J., Fu J., Luo J., Liu Z., Wei H. (2016b) An advanced Driller's Method simulator for deepwater well control, *J. Loss Prevent. Proc.* **39**, 131–140.

Fu J., Su Y., Jiang W., Li S., Chen Y. (2019) Wellbore annulus water hammer pressure prediction based on transient multiphase flow characteristics, *Oil Gas Sci. Technol. – Rev. IFP Energies nouvelles* **74**, 84.

Gao Y., Cui Y., Xu B., Sun B., Zhao X., Li H., Chen L. (2017) Two phase flow heat transfer analysis at different flow patterns in the wellbore, *Appl. Therm. Eng.* **117**, 544–552.

Guo R., Chen Y., Waltrich P.J., Williams W.C. (2018) An experimental investigation on flow pattern map and drift-flux model for Co-Current upward liquid-gas two-phase flow in narrow annuli, *J. Nat. Gas. Sci. Eng.* **51**, 65–72.

Guo X., Wang Q. (2016) A new prediction model of elemental sulfur solubility in sour gas mixtures, *J. Nat. Gas Sci. Eng.* **31**, 98–107.

Hasan A.R., Kabir C.S. (1988) A study of multiphase flow behavior in vertical wells, *Spede.* **3**, 2, 263–272. https://doi.org/10.2118/15138-PA.

Hou Z., Yan T., Li Z., Feng J., Sun S., Yuan Y. (2019) Temperature prediction of two phase flow in wellbore using modified heat transfer model: An experimental analysis, *Appl Therm. Eng.* **149**, 54–61.

Kelessidis V.C., Dukler A.E. (1989) Modeling flow pattern transitions for upward gas-liquid flow in vertical concentric and eccentric annuli, *Int. J. Multiphase Flow.* **15**, 2, 173–191.

Li H.Z., Mouline Y. (1997) Chaotic bubble coalescence in non-newtonian fluids, *Int. J. Multiphase Flow.* **23**, 713–723.

Mao L., Zhang Z. (2018) Transient temperature prediction model of horizontal wells during drilling shale gas and geothermal energy, *J. Petrol. Sci. Eng.* **169**, 610–622.

Meng Y., Xu C., Na W., Gao L., Hongtao L., Mubai D. (2015) Numerical simulation and experiment of the annular pressure variation caused by gas kick/injection in wells, *J Nat Gas Sci Eng.* **22**, 646–655.

Nickens H.V. (1987) A dynamic computer model of kick Well, *SPE Drill. Eng.* **2**, 2, 158–173. https://doi.org/10.2118/14183-PA.

Osman E.S.A. (2004) Artificial neural network models for identifying flow regimes and predicting liquid holdup in horizontal multiphase flow, *SPE Prod. Facil.* **19**, 1, 33–40. https://doi.org/10.2118/68219-MS.

Rader D.W., Bourgoyne A.T., Ward R.H. (1975, May 1) *Factors affecting bubble-rise velocity of gas kicks*, Society of Petroleum Engineers. https://doi.org/10.2118/4647-PA.

Raghavan R. (1989) Well-test analysis for multiphase flow, *SPE Form. Eval.* **4**, 4, 585–594. https://doi.org/10.2118/14098-PA.

Shi H., Li G., Huang Z., Shi S. (2014) Properties and testing of a hydraulic pulse jet and its application in offshore drilling, *Petrol. Sci.* **11**, 3, 401–407.

Sun B., Gong P.B., Wang Z.Y. (2013) Simulation of gas kick with high H_2S content in deep well, *J. Hydrodyn.* **25**, 2, 264–273.

Sun B.J., Sun X.H., Wang Z.Y., Chen Y.H. (2017) Effects of phase transition on gas kick migration in deepwater horizontal drilling, *J. Nat. Gas Sci. Eng.* **46**, 710–729.

Sun B.J., Guo Y.H., Sun W.T., Gao Y., Hao L., Wang Z., Zhang H. (2018) Multiphase flow behavior for acid-gas mixture and drilling fluid flow in vertical wellbore, *J. Petrol. Sci. Eng.* **165**, 388–396.

Vesovic V., Assael M.J., Gallis Z.A. (1998) Prediction of the viscosity of supercritical fluid mixtures, *Int. J. Thermophys.* **19**, 5, 1297–1313.

Wang N., Sun B., Wang Z., Wang J., Yang C. (2016) Numerical simulation of two phase flow in wellbores by means of drift flux model and pressure based method, *J. Nat. Gas. Sci. Eng.* **36**, 811–823.

Wang Z.Y., Sun B.J. (2014) Deepwater gas kick simulation with consideration of the gas hydrate phase transition, *J. Hydrodyn.* **26**, 1, 94–103.

Wang Z., Sun B. (2009) Annular multiphase flow behavior during deep water drilling and the effect of hydrate phase transition, *Petrol. Sci.* **6**, 1, 57–63.

Wei N., Xu C.Y., Meng Y.F., Li G. (2018) Numerical simulation of gas-liquid two-phase flow in wellbore based on drift flux model, *Appl. Math. Comput.* **338**, 175–191.

Xu Z.M., Song X.Z., Li G.S., Wu K., Pang Z., Zhu Z. (2018) Development of a transient non-isothermal two-phase flow model for gas kick simulation in HTHP deep well drilling, *Appl. Therm. Eng.* **141**, 1055–1069.

Xu Z.M., Song X.Z., Li G.S., Zhu Z., Zhu B. (2019) Gas kick simulation in oil-based drilling fluids with the gas solubility effect during high-temperature and high-pressure well drilling, *Appl. Therm. Eng.* **149**, 1080–1097.

Xie J., Zhang X., Tang Y., Wang Y., Shao Q., Yu B. (2014) Transient simulation of the blowing-out process of the air pockets in vertical wellbore, *Appl. Therm. Eng.* **72**, 97–103.

Yin H., Liu P., Li Q., Wang Q., Gao D. (2015) A new approach to risk control of gas kick in high-pressure sour gas wells, *J. Nat. Gas Sci. Eng.* **26**, 142–148.

Yin B., Gang L., Li X. (2017) Multiphase transient flow model in wellbore annuli during gas kick in deepwater drilling based on oil-based mud, *Appl. Math. Model.* **51**, 159–198.

Zhang X., Li Q., Zheng L., Li X., Xu L. (2020) Numerical simulation and feasibility assessment of acid gas injection in a carbonate formation of the Tarim Basin, China. Oil Gas, *Sci. Technol.* **75**, 1–17.

Zhang J., Li X., Tang X., Luo W. (2019) Establishment and analysis of temperature field of riserless mud recovery system, *Oil Gas Sci. Technol. – Rev. IFP Energies nouvelles* **74**, 19.

Zhu G., Zhang S., Huang H., Liang Y., Meng S., Li Y. (2011) Gas genetic type and origin of hydrogen sulfide in the Zhongba gas field of the western Sichuan Basin, China, *Appl. Geochem.* **26**, 7, 1261–1273.